

Insight into the “synergistic-relaxation effects” in amorphous polymer: Thermodynamic modeling, multiphysics simulation and application in 4D printing

Hao Duan, Huiyu Sun ^{*}, Jesus A. Rodriguez-Morales, Xinyuan Bai

State Key Laboratory of Mechanics and Control of Mechanical Structures, Nanjing University of Aeronautics and Astronautics, Nanjing, China

ARTICLE INFO

Keywords:

4D-printed shape memory polymers
Thermodynamic modeling
Multiphysics simulation
Synergistic-relaxation effects

ABSTRACT

Structure and stress relaxation in shape memory polymers (SMPs), which show the time-dependent response to temperature and mechanical loading, respectively, are usually thought to be the primary mechanisms of shape memory effects (SMEs). However, the synergistic effect of structure and stress relaxation has not been well investigated. What's more, convenient and economic manufacturing and structural customization of SMPs can be easily achieved by four-dimensional (4D) printing technology. Thus, in this paper, we comprehensively analyze the working mechanisms of synergistic-relaxation effects in both traditional and 4D-printed SMPs using theoretical calculations and experimental confirmation. Specifically, the calculations are based on the thermo-mechanical and electro-thermo-mechanical models, and multiple sets of experimental data are used to verify the model results. The model results agree well with the experimental data and demonstrate that synergistic-relaxation mechanisms play an important role in thermo-mechanical behaviors.

1. Introduction

SMPs possess variable mechanical properties and excellent shape memory characteristics, making them applicable to many cutting-edge engineering fields [1,2]. SMPs can be easily programmed to keep a desired shape and recover their initial shape under various external stimuli such as temperature [3,4], light [5,6], electricity [7,8], and magnetic fields [9,10]. The steps of the shape memory cycle include shape programming above the glass transition temperature (T_g), shape fixity (cooling down to below T_g), and shape recovery (reheating to above T_g).

It is generally agreed that the physical mechanisms determining the SMEs are closely related to the structure and stress relaxation [11–20]. Structure relaxation plays an essential role in the glass transition region, which describes the temperature-dependent response for structure. Stress relaxation has an obvious time-dependent response to mechanical loading. Note that differ from the clear impact on the free volume of

polymer by the structure relaxation, stress relaxation has a negligible effect. As a result, the core of the shape memory phenomenon is the time dependence of polymer materials on temperature and mechanical loading. In the glassy region, load-dependent viscoelastic phenomena can be applied to represent the time-dependent response. However, temperature events occur throughout the entire thermo-mechanical cycle, such as shape fixity and shape recovery. The molecular activation energy barrier and its available free volume will be in a state of nonlinear change [11,21]. Thus, the effect of structural relaxation on the viscoelastic phenomenon should be considered in the overall shape memory cycle.

On the other hand, high-temperature programming is not easy to implement in all the engineering applications. Fortunately, polymer-based shape memory materials can also be induced to produce SMEs below T_g . A series of related studies have been conducted [22–30]. The low-temperature shape memory cycle includes shape programming below T_g , shape fixity (stress relaxation), and shape recovery (reheating

* Corresponding author.

E-mail address: hysun@nuaa.edu.cn (H. Sun).

to above T_g). It is clear that temperature events occur only in the shape recovery process. The shape memory capability depends on the sufficient duration of a nonequilibrium thermodynamic state, regardless of the programming temperature [24]. Thus, stress relaxation in the form of viscosity plays the main role in cold programming, and the effect of structure relaxation is not significant enough [30]. We attempt to construct new physical mechanisms to underpin SMEs.

In this paper, the relationship between structure relaxation and stress relaxation is deeply cooperative. We propose a thermodynamic constitutive model incorporating the synergistic-effect mechanisms of structure and stress relaxation. Structure relaxation's effect is incorporated into the stress-activated viscous flow with the help of thermodynamic state variable theory and free volume theory. The change in the activation energy barrier can be expressed by combining the Eyring equation with the Williams-Landel-Ferry (WLF) relationship. Based on this constitutive model, the mechanical and shape memory responses of SMPs are simulated. To better validate the model's universality and robustness, it is extended to research in the field of multiphysics using a new electrothermal model. In addition, the development of 4D printing technology offers a convenient, efficient, and cost-effective method for manufacturing and customizing SMPs. Therefore, the thermodynamic constitutive model is also used to investigate the thermo-mechanical behaviors of 4D-printed SMPs.

This paper's structure includes Sections 2 (thermodynamic modeling), 3 (results and discussions), and 4 (conclusions and future work).

2. Thermodynamic modeling

2.1. Kinematics

As shown in Fig. 1, the overall deformation can be broken down into mechanical and thermal deformations through polar decomposition,

$$\mathbf{F} = \mathbf{F}_M \cdot \mathbf{F}_T \quad (1)$$

where \mathbf{F}_M and \mathbf{F}_T represent the mechanical and thermal deformations. \mathbf{F}_M can be represented by the elastic and viscous deformation,

$$\mathbf{F}_M = \mathbf{F}_e \cdot \mathbf{F}_v \quad (2)$$

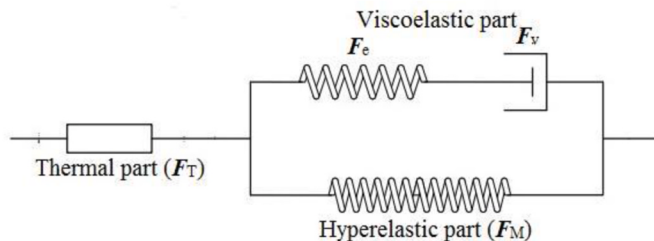


Fig. 1. The brief introduction for the constitutive model.

Table 1
Model parameters fitted by the experiments [26].

Parameters	Values	Parameters	Values
T_g	42.1 °C	ρ	1050 kg/m ³
μ_r	2.2 MPa	n_g	10123 MPa/s
λ_L	4.0	ΔG	4.6×10^{-21} J
Q_s	1899K	C_1	33.9
ν	0.4	C_2	76.1 °C
k_0	$0.6 \times 10^{-4}/^{\circ}\text{C}$	τ_0	1.5s
B	20000J/kg	η_{ref}	6.0J/Kg-K
C_{p0}	50J/Kg-K	κ	1.0
e	1.5×10^{-9} J/kg-K	d	1.5×10^{-17} J/kg
w_t	1.0×10^{-16} kg/m ³	v_t	5.0×10^{-16} kg/m ³
T_{ref}	25 °C	E	463.2 MPa
s_0, s_s	16.77 MPa, 11.05 MPa	h_0	170 MPa

Table 2
Model parameters fitted by the experiments [15,40].

Parameters	Values [15,40]	Parameters	Values [15,40]
T_g	40 °C, 75 °C	ρ	1050 kg/m ³
μ_r	0.179 MPa, 0.58 MPa	n_g	60 MPa/s, 15 MPa/s
λ_L	1.14, 1.75	ΔG	4.6×10^{-21} J, 5.0 × 10^{-20} J
Q_s	9625 K, 12897.5 K	C_1	17.44
ν	0.4	C_2	51.6 °C, 77.6 °C
k_0	$1.25 \times 10^{-4}/^{\circ}\text{C}$, 0.68 × $10^{-4}/^{\circ}\text{C}$	τ_0	0.03s, 15s
B	20000J/kg	η_{ref}	6.0J/Kg-K, 4.0J/Kg-K
C_{p0}	50J/Kg-K	κ	1.0
e	1.5×10^{-9} , 0.5 × 10^{-9} J/ $\text{Kg}\cdot\text{K}$	d	1.5×10^{-17} , 4.5 × 10^{-18} J/Kg
w_t	1.0×10^{-16} kg/m ³	v_t	5.0×10^{-16} , 6.5 × 10^{-16} kg/m ³
T_{ref}	25 °C	E	463.2 MPa, 1799 MPa
s_0, s_s	55, 73.7 MPa; 35, 40.2 MPa	h_0	700 MPa, 390 MPa

where "e" symbolizes elasticity, and "v" symbolizes viscosity.

The isotropic thermal deformation gradient is written as:

$$\mathbf{F}_T = J_T^{1/3} \mathbf{I} \quad (3)$$

where J_T symbolizes the volume deformation related to temperature.

The related deformation tensors are written as:

$$\mathbf{B}_M = \mathbf{F}_M \cdot \mathbf{F}_M^T \quad (4)$$

$$\mathbf{B}_e = \mathbf{F}_e \cdot \mathbf{F}_e^T \quad (5)$$

$$\mathbf{B}_v = \mathbf{F}_v \cdot \mathbf{F}_v^T \quad (6)$$

$$\mathbf{E}_M = \frac{1}{2} (\mathbf{C}_M - \mathbf{I}) \quad (7)$$

The tensor conversion relationship is represented by,

$$\mathbf{B}_e = \mathbf{F}_M \cdot (\mathbf{F}_v^T \cdot \mathbf{F}_v)^{-1} \cdot \mathbf{F}_M^T \quad (8)$$

where I denotes as the identity tensor.

2.2. Stress relations

The hyperelastic stress response can be well represented by the model reported in the literature [31],

Table 3
Model parameters fitted by the cyclic mechanical experiment [42].

Parameters	Values	Parameters	Values
T_g	42.7 °C	ρ	1050 kg/m ³
μ_r	1.7 MPa	n_g	12 MPa/s
λ_L	4.0	ΔG	5.0×10^{-20} J
Q_s/s_y	175K/MPa	C_1	10.44
ν	0.4	C_2	51.6 °C

Table 4
Model parameters fitted by the experiments [43].

Parameters	Values	Parameters	Values
T_g	55 °C	ρ_{CNP}	105.3 kg/m ³
μ_r	0.95 MPa	n_g	4.0 MPa/s
λ_L	1.75	ΔG	5.0×10^{-20} J
Q_s/s_y	1550K/MPa	C_1	26.33
ν	0.4	C_2	101.37 °C
ρ_m	1186 kg/m ³	k_m	0.15 W·m-K
$C_{p\text{CNP}}$	710 J/kg-K	E_{matrix} , E_{CNP}	599 MPa, 680 MPa
k_0	$1.0 \times 10^{-4}/^{\circ}\text{C}$	r_{CNP}	666S/m

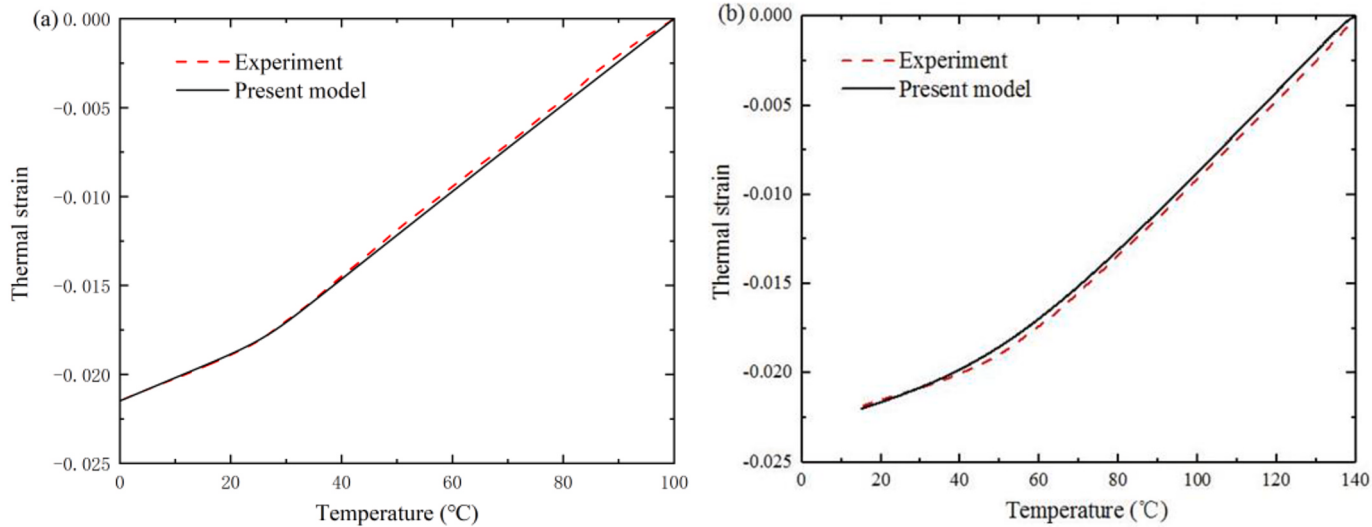


Fig. 2. Thermal strain of (a) the traditional SMP in Ref. [15] and (b) the traditional SMP in Ref. [40] for stress-free at a constant cooling rate.

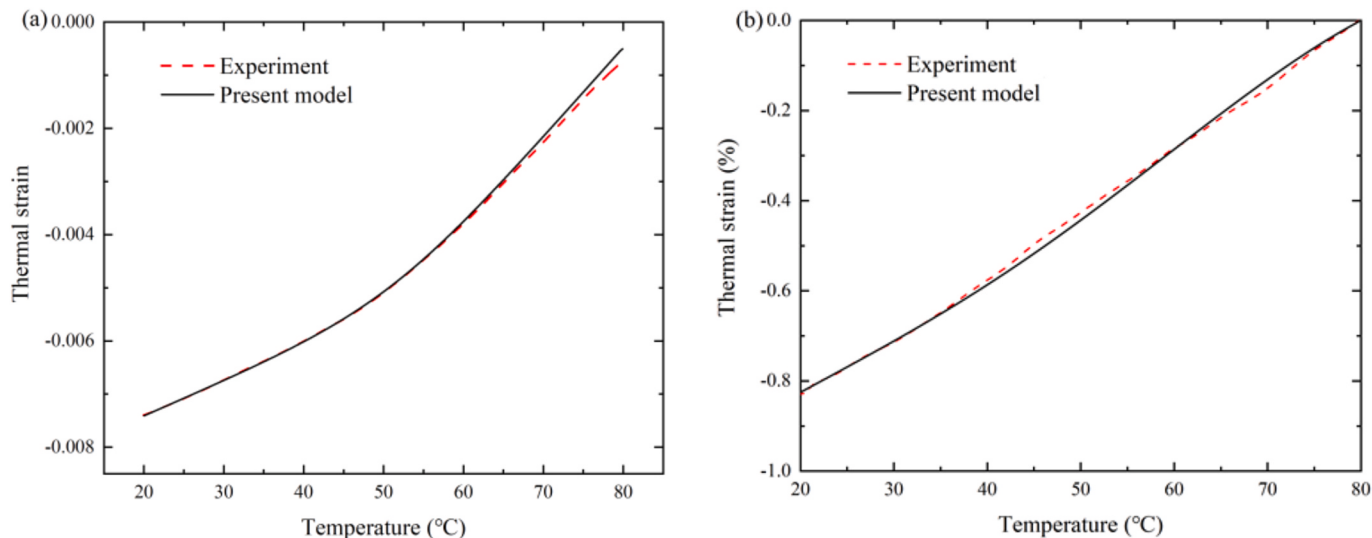


Fig. 3. Thermal strain of (a) the 4D-printed SMP in Ref. [1] and (b) the 4D-printed SMP Ref [41] for stress-free at a constant cooling rate.

$$\sigma_M = \frac{\mu_r}{J_M} \frac{\lambda_L}{\lambda_{\text{eff}}} L^{-1} \left(\frac{\lambda_{\text{eff}}}{\lambda_L} \right) \left(\bar{\mathbf{B}}_M - \frac{1}{3} \bar{I}_M \mathbf{I} \right) \quad (9)$$

where μ_r is the modulus in rubbery state, λ_L and λ_{eff} are the related physical parameters. The stress response of the implicit spring is characterized by the neo-Hookean model,

$$\sigma_e = \frac{1}{J_M} G_e \left(\bar{\mathbf{B}}_e - \frac{1}{3} \bar{I}_e \mathbf{I} \right) \quad (10)$$

where G_e is the nonequilibrium spring stiffness. The total Cauchy stress is expressed as:

$$\sigma = \frac{\mu_r}{J_M} \frac{\lambda_L}{\lambda_{\text{eff}}} L^{-1} \left(\frac{\lambda_{\text{eff}}}{\lambda_L} \right) \left(\bar{\mathbf{B}}_M - \frac{1}{3} \bar{I}_M \mathbf{I} \right) + \frac{1}{J_M} G_e \left(\bar{\mathbf{B}}_e - \frac{1}{3} \bar{I}_e \mathbf{I} \right) \quad (11)$$

where $\bar{I}_e = \text{tr}(J_e^{-2/3} \mathbf{B}_e)$, $\bar{I}_e = \text{tr}(J_e^{-2/3} \mathbf{B}_e)$ and $\bar{I}_M = \text{tr}(J_M^{-2/3} \mathbf{B}_M)$. Equations (9)–(11) can be obtained with the restrictions of the second law of thermodynamics. For convenience, the detailed thermodynamic derivation process is placed in [Appendix A](#).

The tensor B_e evolution takes the following form, utilizing the Lie derivative [32],

$$L_v \mathbf{B}_e = -2 \mathbf{F}_e \cdot \mathbf{D}_v \cdot \mathbf{F}_e^T \quad (12)$$

$$\mathbf{D}_v = \mathbf{F}_v \cdot \mathbf{F}_v^{-1} \quad (13)$$

where \mathbf{D}_v is the rate of stretching tensor.

2.3. Synergistic-relaxation

2.3.1. Time-dependent response to temperature

In the previous study [17], the internal thermodynamic state variable approach is successfully applied to describe the structure relaxation. In the equilibrium state, T_{ref} , η_{ref} and $\alpha_{i\text{ref}}$ ($i = 1, 2, \dots, n$) are regarded as reference values of the temperature T , the specific entropy of unit mass η , and the set of internal thermodynamic variables tensor α_i ($i = 1, 2, \dots, n$), respectively. The degree of deviation from equilibrium is able to be described by the sufficiently small fluctuations of the variables, which gives:

$$T = T_{\text{ref}} + \vartheta(t) \quad (14)$$

$$\eta = \eta_{\text{ref}} + \Delta\eta(t) \quad (15)$$

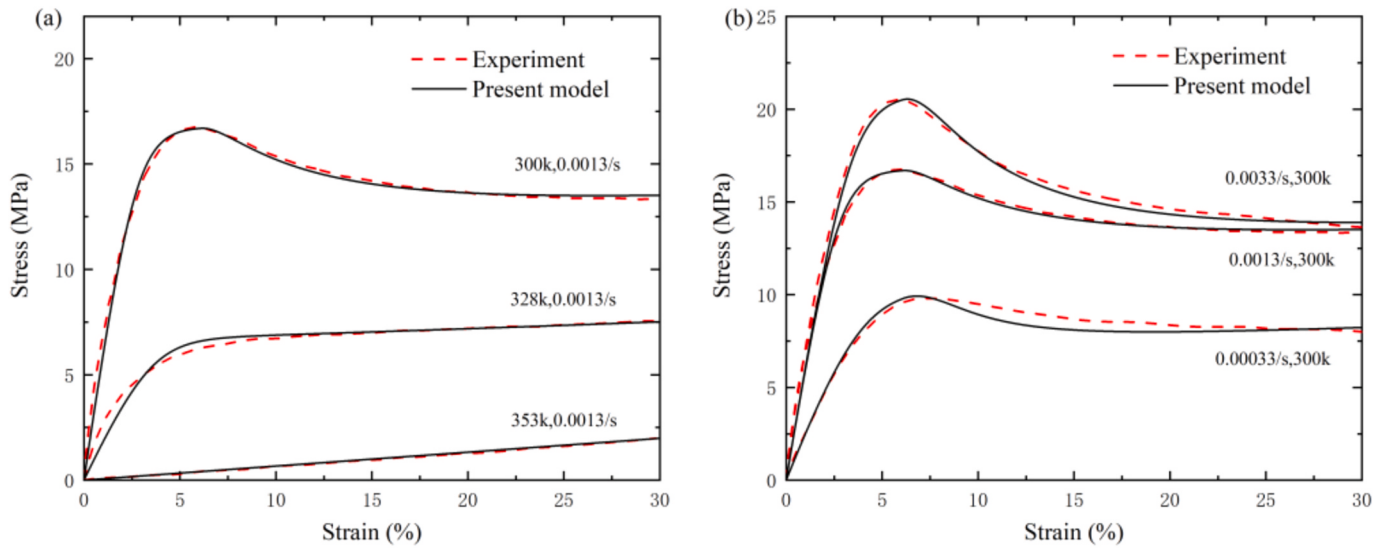


Fig. 4. Stress-strain curves at different (a) strain rates and (b) temperatures [26].

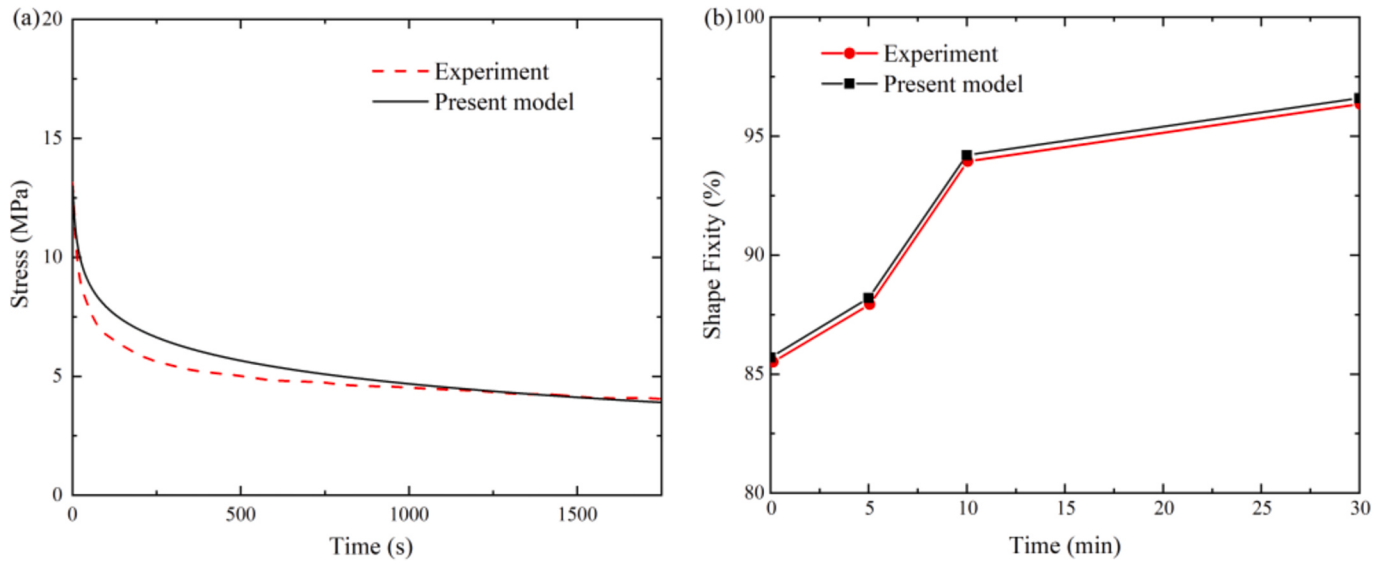


Fig. 5. (a) Stress relaxation and (b) shape fixity [26].

$$\alpha = \alpha_{\text{ref}} + \delta(t) \quad (16)$$

where $\delta(t)$, $\Delta\eta(t)$ and α_{ref} have time dependence.

In the work of Lion et al. [33,34], the basic thermodynamic perturbation functions for the specific entropy and the internal thermodynamic state variable are defined as:

$$\Delta\eta = \frac{c_{p0}}{T_{\text{ref}}} \vartheta - \mathbf{e} \cdot \{\delta\} \quad (17)$$

$$\{\delta\} = -\frac{1}{\tau_R} \left(\{\delta\} + \frac{\mathbf{e}}{d} \vartheta \right) \quad (18)$$

where c_{p0} is the specific heat, ρ is the density, \mathbf{e} is the parameter vectors that can be expressed as

$$\mathbf{e} = [e \ e \ e \ 0 \ 0 \ 0]^T \quad (19)$$

\mathbf{w} is the additional material parameters of the polymer matrix, i.e.,

$$\mathbf{w} = \begin{bmatrix} w_t & v_t & v_t & 0 & 0 & 0 \\ v_t & w_t & v_t & 0 & 0 & 0 \\ v_t & v_t & w_t & 0 & 0 & 0 \\ 0 & 0 & 0 & w_s & 0 & 0 \\ 0 & 0 & 0 & 0 & w_s & 0 \\ 0 & 0 & 0 & 0 & 0 & w_s \end{bmatrix} \quad (20)$$

where w_t , v_t and w_s are represent the coupling parameters between the internal thermodynamic variable and the stress. The structure relaxation function τ_R is described by the Adam–Gibbs model [21] as follows:

$$\tau_R = \tau_0 \exp\left(\frac{B}{T(\eta_{\text{ref}} + \Delta\eta(t))}\right) \quad (21)$$

where τ_0 is the reference structure relaxation time and B is the activation parameter.

The thermal strain is represented as

$$\{\epsilon_T\} = k_0 \vartheta - \rho \mathbf{w} \{\delta\} \quad (22)$$

k_0 is the parameter vectors that can be expressed as

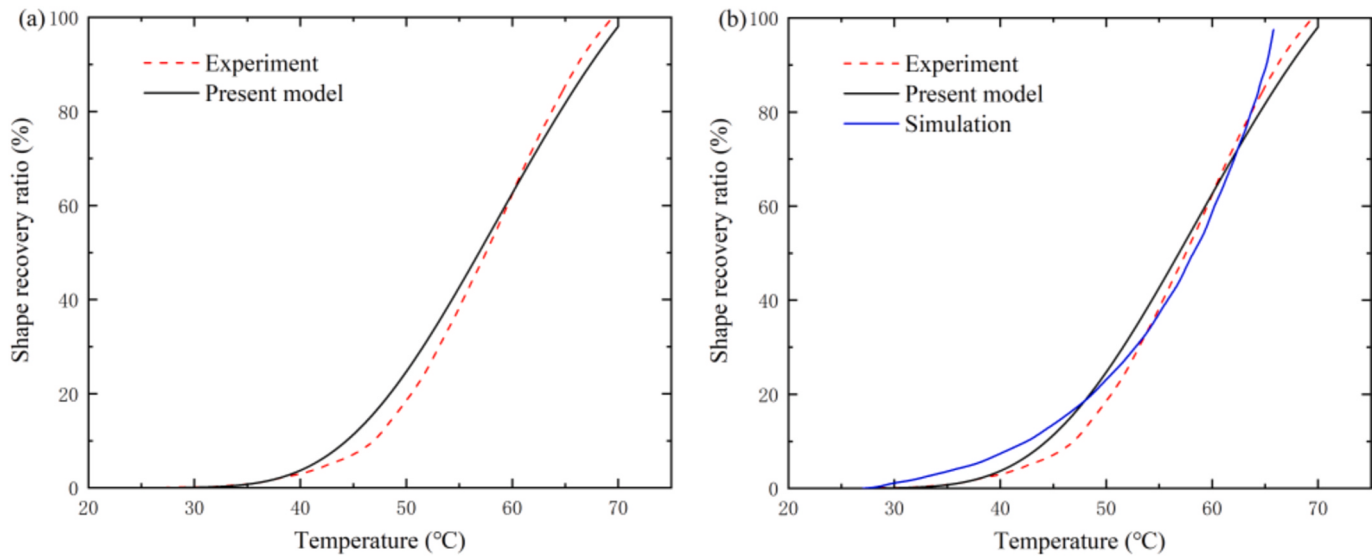


Fig. 6. Comparing the shape recovery response represented by the present model with the (a) experimental data [26] and the (b) simulation [26].

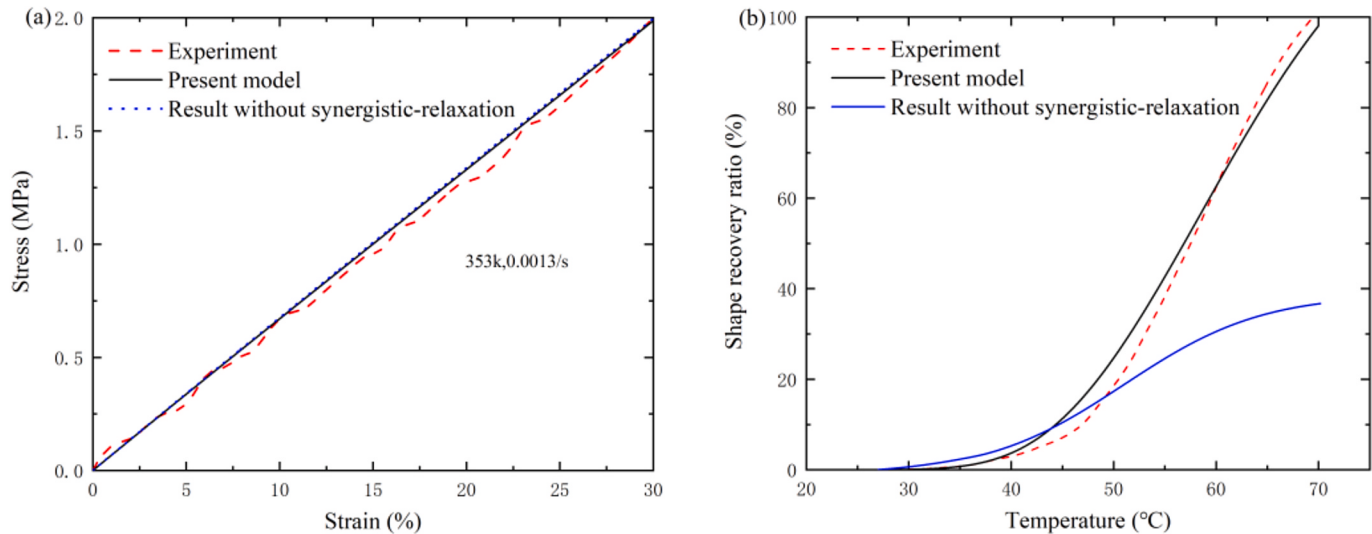


Fig. 7. The effects of synergistic-relaxation on the (a) mechanical response and the (b) shape recovery response [26].

$$\mathbf{k}_0 = [k_0 \ k_0 \ k_0 \ 0 \ 0 \ 0]^T \quad (23)$$

where k_0 represents the thermal expansion coefficient (CTE) in glassy state. Accordingly, the thermal volume strain $\varepsilon_{T,V}$ is calculated by taking Eqs. (20), (22) and (23) into account, i.e.,

$$\varepsilon_{T,V} = 3k_0\theta - \rho(w_t + 2\nu_t)(\delta_1 + \delta_2 + \delta_3) \quad (24)$$

Therefore, the initial value of the thermal volume strain is written as

$$\varepsilon_{T,V}^0 = 3k_0(T_0 + T_{ref}) - \rho(w_t + 2\nu_t)(\delta_1^0 + \delta_2^0 + \delta_3^0) \quad (25)$$

where T_0 is the initial temperature, δ_1^0 , δ_2^0 and δ_3^0 are the initial values of the internal thermodynamic state variable. Thus, the thermal deformation J_T is given by

$$J_T = 1 + \varepsilon_{T,V} - \varepsilon_{T,V}^0 \quad (26)$$

2.3.2. Viscous flow rule

The tensor D_V can be expressed as:

$$D_V = \frac{d\gamma_V}{dt} n \quad (27)$$

where $d\gamma_V/dt$ is the plastic shear strain rates [13,35]. This section uses the Eyring model to characterize $d\gamma_V/dt$,

$$\frac{d\gamma_V}{dt} = \frac{s_y}{n_g} \frac{T}{Q_s} \exp\left(-\frac{\Delta G}{k_B T}\right) \sinh\left(\frac{Q_s \bar{\tau}}{T s_y}\right) \quad (28a)$$

where s_y is the stress related to the yield, η_g is the reference shear viscosity at T_g . $\bar{\tau}$ is defined as follows.

$$\bar{\tau} = \sqrt{\frac{1}{2} \sigma_e : \sigma_e} \quad (28b)$$

The influences of the nonlinear variation of activation energy and free volume related to the temperature should be incorporated into the viscous flow rule. $\Delta G(T)$ can be calculated by:

$$\Delta G(T) = \Delta G(T_g) \cdot 10^{\frac{-C_1(T-T_g)}{C_2+T-T_g}} \quad (29)$$

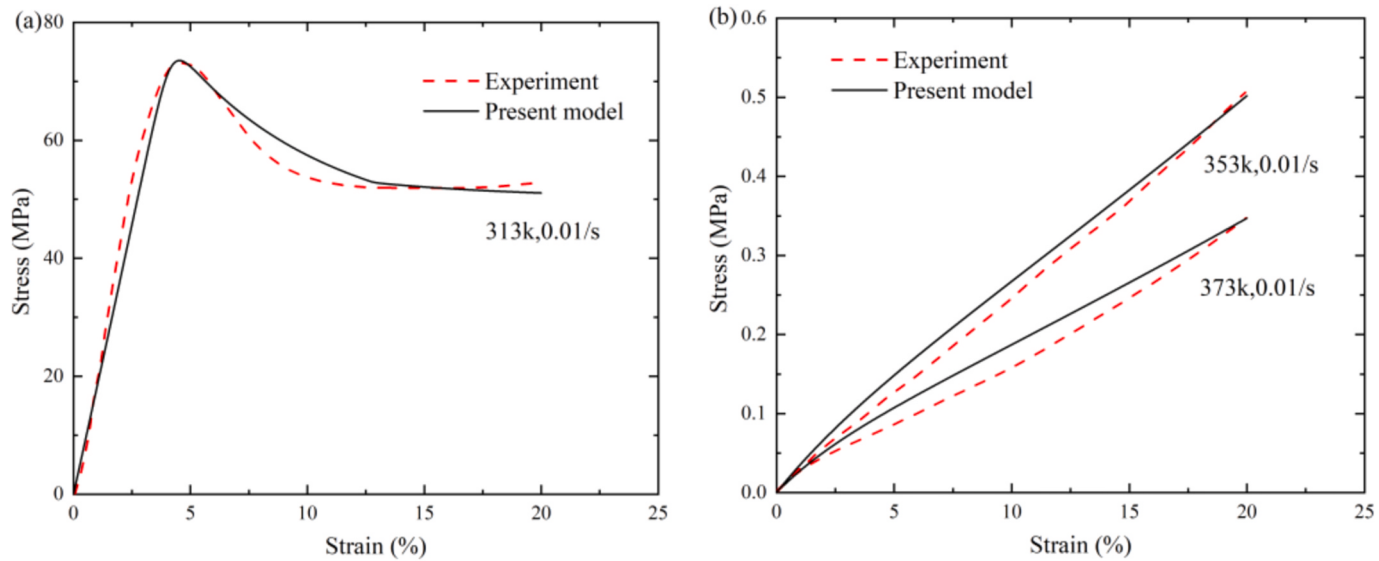


Fig. 8. Stress-strain curves at different temperatures under a compression strain of 20 % [40].

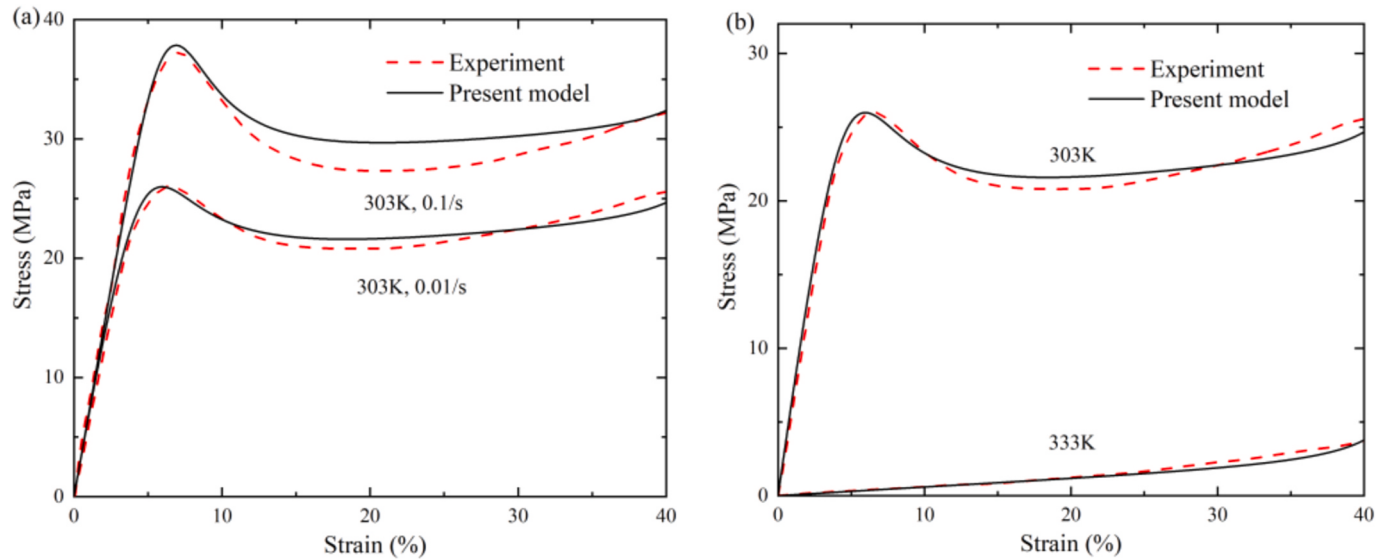


Fig. 9. Stress-strain curves at different (a) strain rates and (b) temperatures under a compression strain of 40 % [15].

where C_1 and C_2 are the WLF constants. The probability of SMP to obtain enough free volume available to jump can be expressed by the following form [36]:

$$z_v = \exp\left(-\frac{\kappa V_0}{V_f}\right) \quad (30a)$$

where κ is a given constant from 0.5 to 1, V_0 is the volume of the occupied molecules and V_f is the free volume in polymer. Based on the Doolittle equation [37,38], V_f is fully resulted from thermal expansion at the constant pressure:

$$V_f = V_0 \left\{ \exp \left[\int_0^T \alpha(T) dT \right] - 1 \right\} \quad (30b)$$

where $\alpha(T)$ is the coefficient of thermal expansion related to temperatures. Therefore, the effect of structural relaxation on the viscous flow can be written as Eq. (31).

$$\frac{d\gamma_v}{dt} = \frac{s_y}{n_g} \frac{T}{Q_s} \exp\left(-\frac{\Delta G(T_g) \cdot 10^{-C_2 + T - T_g}}{k_b T}\right) \exp\left(-\frac{\kappa V_0}{V_f}\right) \sinh\left(\frac{Q_s \bar{\tau}}{T s_y}\right) \quad (31)$$

The evolution rule [39] for the post-yield softening behavior is written as

$$\frac{ds_y}{dt} = h_0 \left(1 - \frac{s_y}{s_s}\right) \frac{d\gamma_v}{dt} \quad (32)$$

where s_s is the steady value of s_y .

3. Results and discussions

The simulation is implemented by the C++ platform. The rationality of the model is confirmed using thermo-mechanical experiments [1,15, 26,40–45] with different pre-deformation temperatures. Theoretical calculation parameters are shown in Tables 1–4.

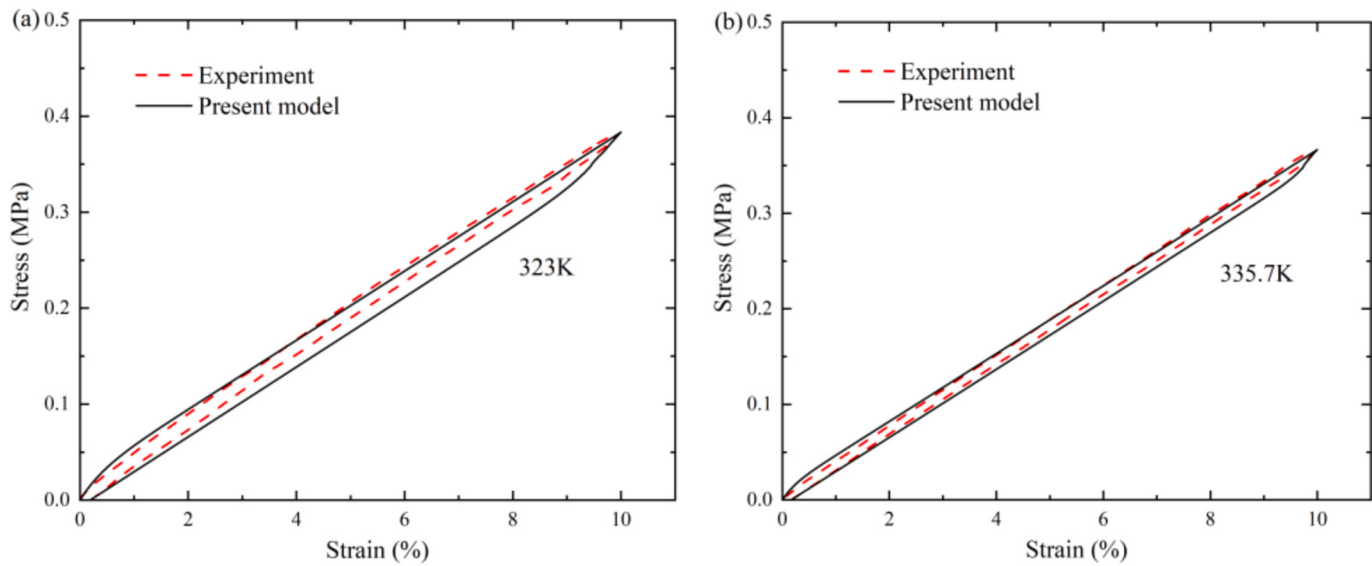


Fig. 10. Cyclic mechanical response of SMP [42]: (a) at 323 k and (b) at 335.7 k.

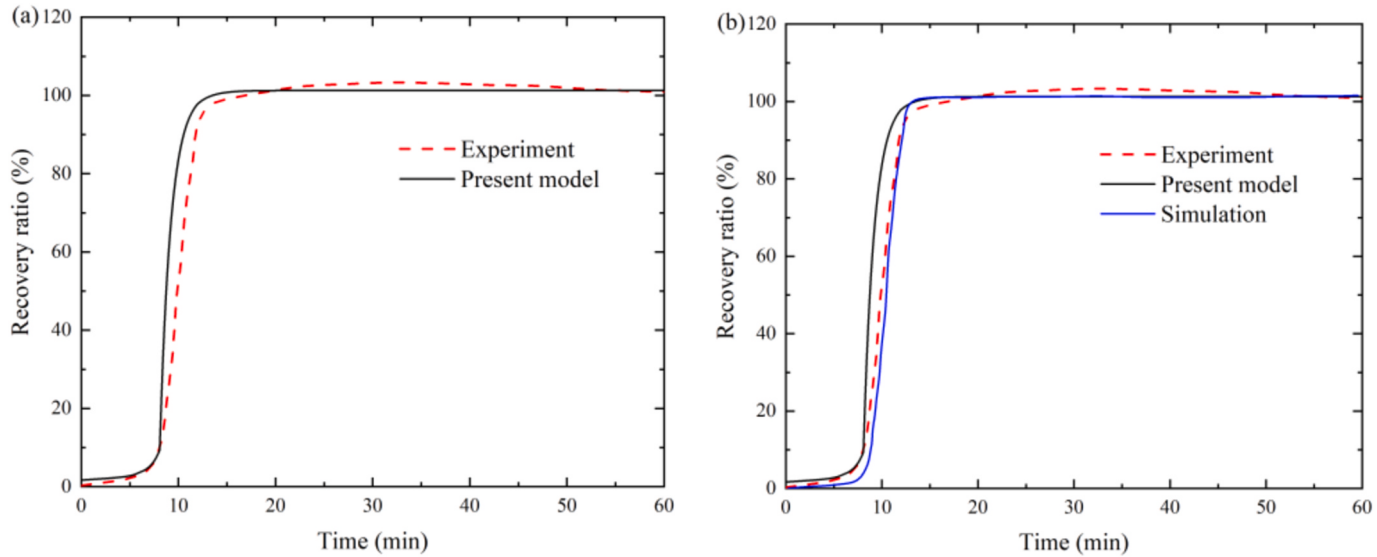


Fig. 11. Comparing the shape recovery response represented by the present model with the (a) experimental data [15] and the (b) simulation [15].

3.1. Parameters determination

As shown in Fig. 2, two sets of thermal expansion experiments of traditional SMPs are conducted by reducing the temperature from 373 K to 273 K in 100 min and the temperature from 413 K to 288 K in 50 min, respectively. Fig. 3 shows two sets of thermal expansion experiments of 4D-printed SMPs, which are both conducted by changing the temperature from 293 K to 353 K in 30 min. Linear regression analysis of the thermal strain curves was conducted to determine $k_1 = 2.52 \times 10^{-4}/^\circ\text{C}$ and $k_0 = 1.25 \times 10^{-4}/^\circ\text{C}$ in Fig. 2a, $k_1 = 2.24 \times 10^{-4}/^\circ\text{C}$ and $k_0 = 0.68 \times 10^{-4}/^\circ\text{C}$ in Fig. 2b, $k_1 = 1.495 \times 10^{-4}/^\circ\text{C}$ and $k_0 = 0.65 \times 10^{-4}/^\circ\text{C}$ in Fig. 3a, and $k_1 = k_0 = 1.11 \times 10^{-4}/^\circ\text{C}$ in Fig. 3b, respectively. The theoretical predictions are also shown in Figs. 2 and 3, and the simulations are in good agreement with the experiments.

The parameters μ_r and λ_L can be obtained by simulating the stress-strain curve above T_g . The appropriate values of viscous parameters Q_s , n_g , s_0 , s_s , h_0 , ΔG can be ascertained by simulating the stress-strain relationship in the glassy temperature region, as depicted in Figs. 5, 9, 12 and 13. More precisely, the estimation of s_0 can be derived from the

stress at the point of yielding, while the saturation value s_s can be determined when the stress-strain curve levels out. The parameter h_0 represents the rate at which strain softening occurs after yielding, and the initial value of h_0 is equivalent to the slope of the reduction in yield. Based on the relevant studies [1,15,26], the initial values of other viscous parameters can be approximated. The ultimate values of these viscoplastic parameters are determined through the process of fitting the experimental curve.

3.2. Verification I

3.2.1. Example 1: experiments cited from Abishera et al. [26]

In this section, low-temperature shape memory cycle experiments and axial tension experiments are conducted; all the experimental data can be found in Abishera et al. [26]. The SMP material ($T_g = 42.1\text{ }^\circ\text{C}$) used in this section is a diglycidyl ether of bisphenol A (DGEBA-Araldite LY556). Uniaxial tension experiments were conducted at different strain rates and temperatures, as presented in Fig. 4. In the cycle experiments, the SMP sample was first programmed to a tensile strain of 30 % at 300 K

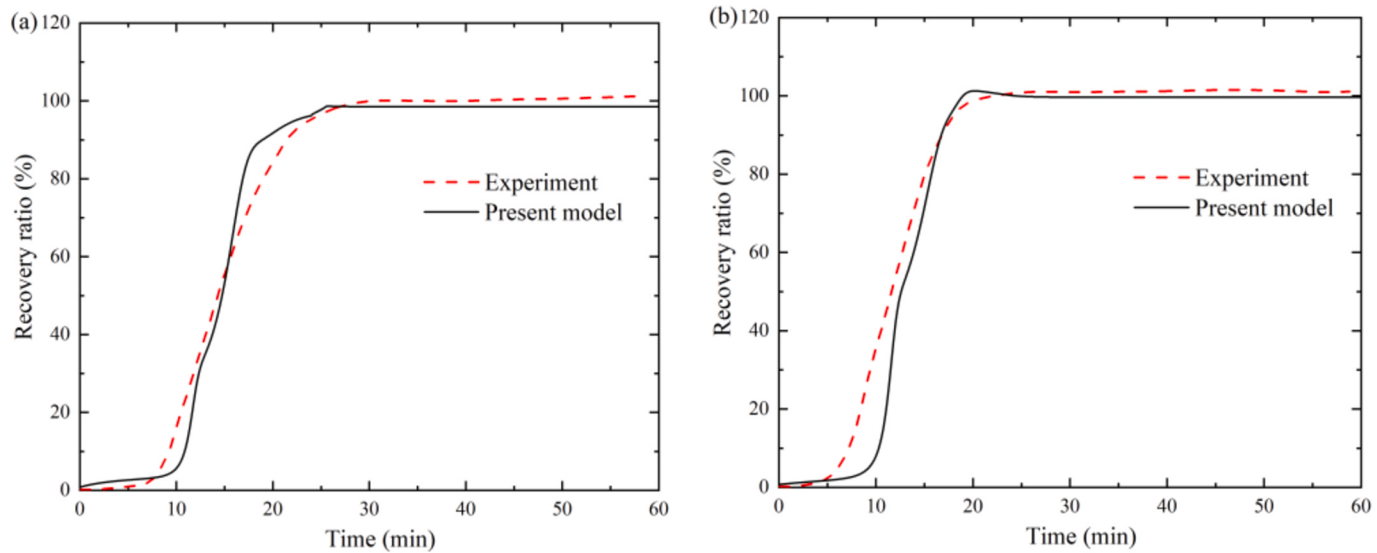


Fig. 12. Shape recovery response of (a) SMP materials [40] with programming temperature 373 K and (b) SMP materials [40] with programming temperature 353 K.

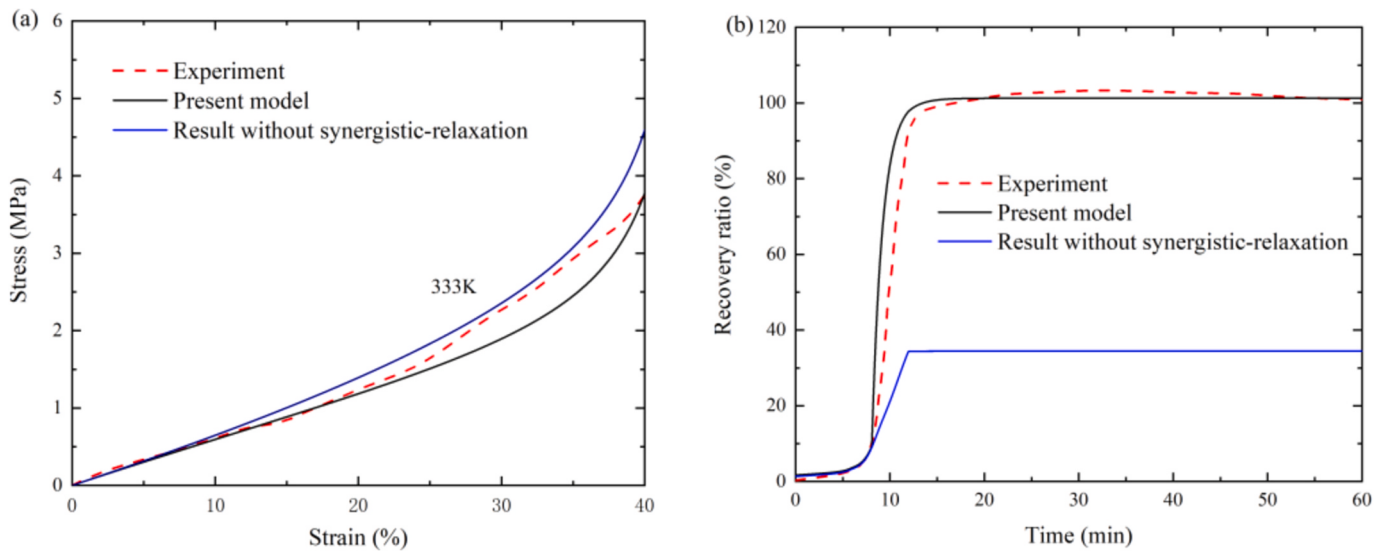


Fig. 13. The effects of synergistic-relaxation on the (a) mechanical response and the (b) shape recovery response [15].

using a strain rate of 0.0013/s. Subsequently, the sample was maintained in the temporary shape for 1800 s to achieve shape fixity. Finally, the ambient temperature was raised to 343 K for the shape recovery at a rate of 3 °C/min. The relevant model parameters are shown in Table 1.

3.2.2. Model results comparing to experiments

Fig. 4 depicts the impact of temperatures and strain states on the axial tension, as simulated through the constitutive model. Temperature and strain rate have a negative and positive relationship with the overall stress value, respectively. In addition, an increase in strain rate

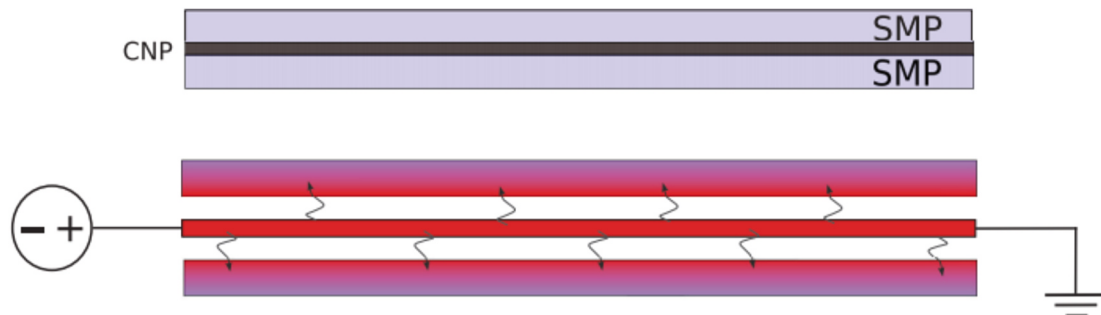


Fig. 14. Electro-active CNP-SMP composite structure [43].

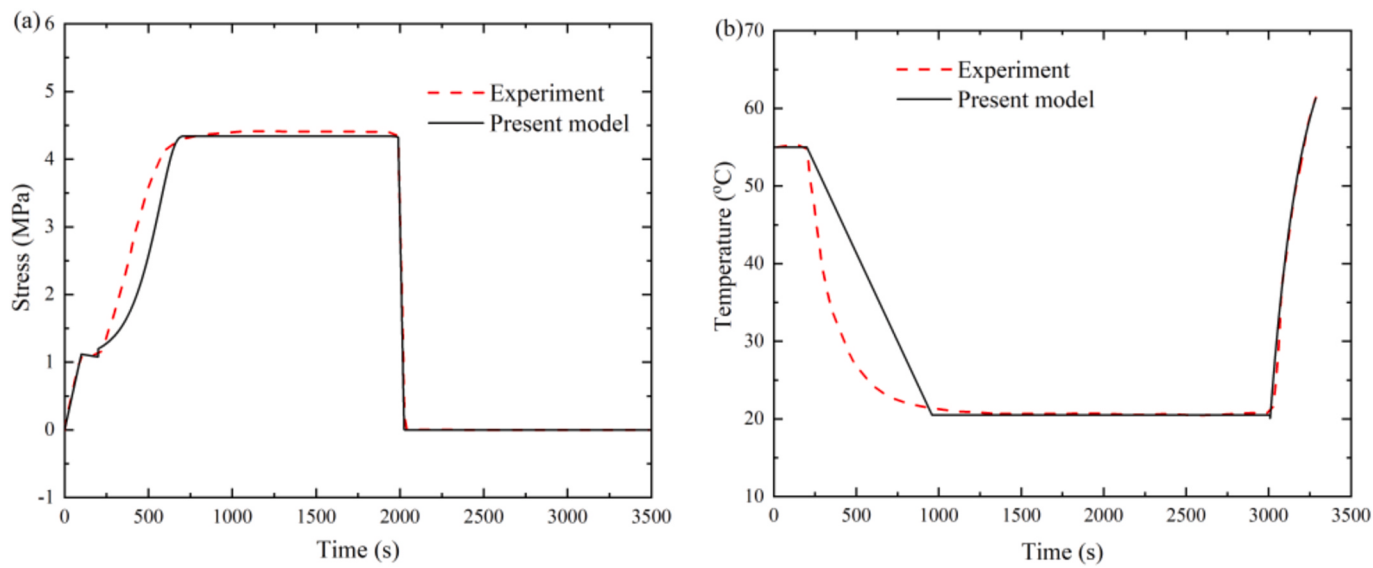


Fig. 15. Comparison of (a) stress and (b) surface temperature between present model and experimental testing [43] in the electro-thermo-mechanical cycle.

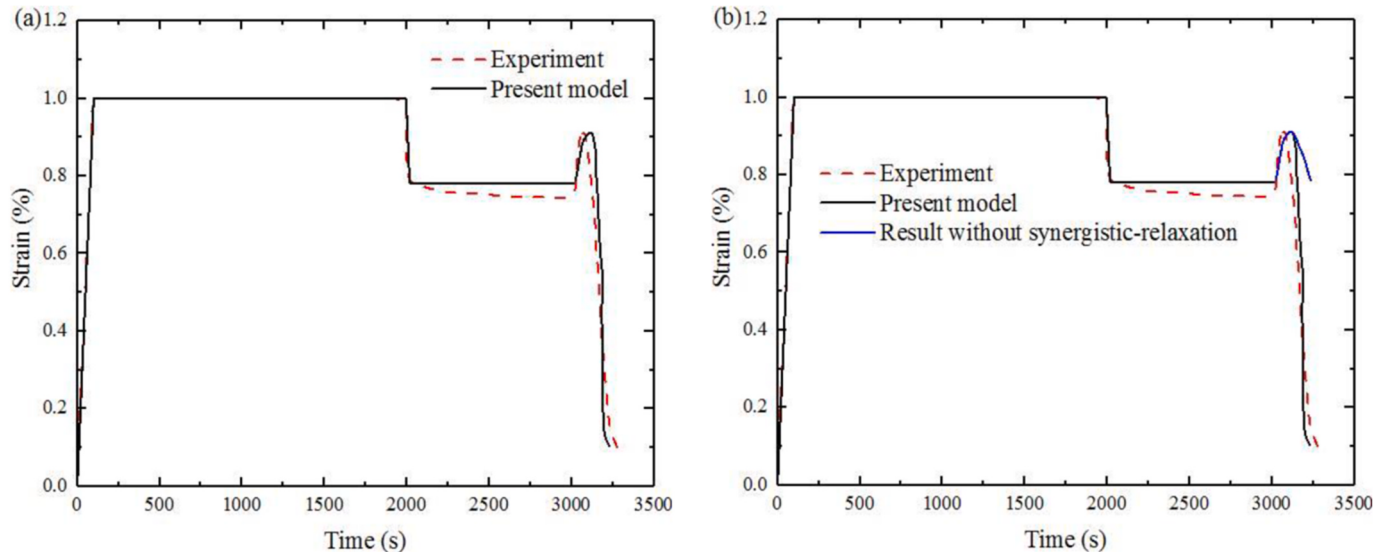


Fig. 16. The effects of synergistic-relaxation on the strain response in the electro-thermo-mechanical cycle [43].

significantly enhances yield strength, while an increase in temperature promotes the disappearance of the viscoplastic response. These thermo-mechanical features can be well captured by the constitutive model.

Fig. 5a illustrates the stress relaxation behavior. The stress rapidly decreases within the first 200 s, but after 1500 s, no further relaxation is noticed. Fig. 5b shows the influence of the relaxation time on the shape fixity. A longer stress relaxation time reduces the reversible strain that can recover instantly during the unloading process, resulting in an increase in shape fixity. The constitutive model successfully captures the stress relaxation character and predicts the shape fixity ratio.

Fig. 6 depicts a stress-free form of recovery. The recovery process initiates at T_g and significantly accelerates in the rubbery temperature region, ultimately leading to an almost full shape recovery. Effective predictions are provided by both the present model and the model in reference 26. However, our constitutive model can represent the shape recovery response more reasonably, as shown in Fig. 6b.

Fig. 7a and b, respectively, show the effects of synergistic-relaxation on mechanical and shape recovery responses. It is indicated that the synergistic-relaxation effects plays a vital role in shape recovery,

whereas the mechanical response in a rubbery state is barely influenced.

3.3. Verification II

3.3.1. Example 2: experiments cited from Westbrook et al. [15]

To show the validity of the model in the high-temperature shape memory cycle, we simulate experiments reported by Westbrook et al. [15] in this section. The SMP material ($T_g = 40^\circ\text{C}$) used in this section is an acrylate-based network polymer.

In the testing environment of various temperatures and strain rates, uniaxial compression experiments were performed, as shown in Fig. 9. The high-temperature shape memory cycle experiments include programming, stress relaxation, and cooling and reheating steps. The sample was first programmed to a compression strain of 20 % at 313 K using a strain rate of 0.01/s, followed by a relaxation period of 10 min. Subsequently, the ambient temperature was decreased to 293 K for about 8 min to achieve shape fixity. To recover its shape, the material was reheated to 323 K at a rate of 2.5 $^\circ\text{C}/\text{min}$. and allowed to stabilize. The total duration for both the reheating and stabilization processes is

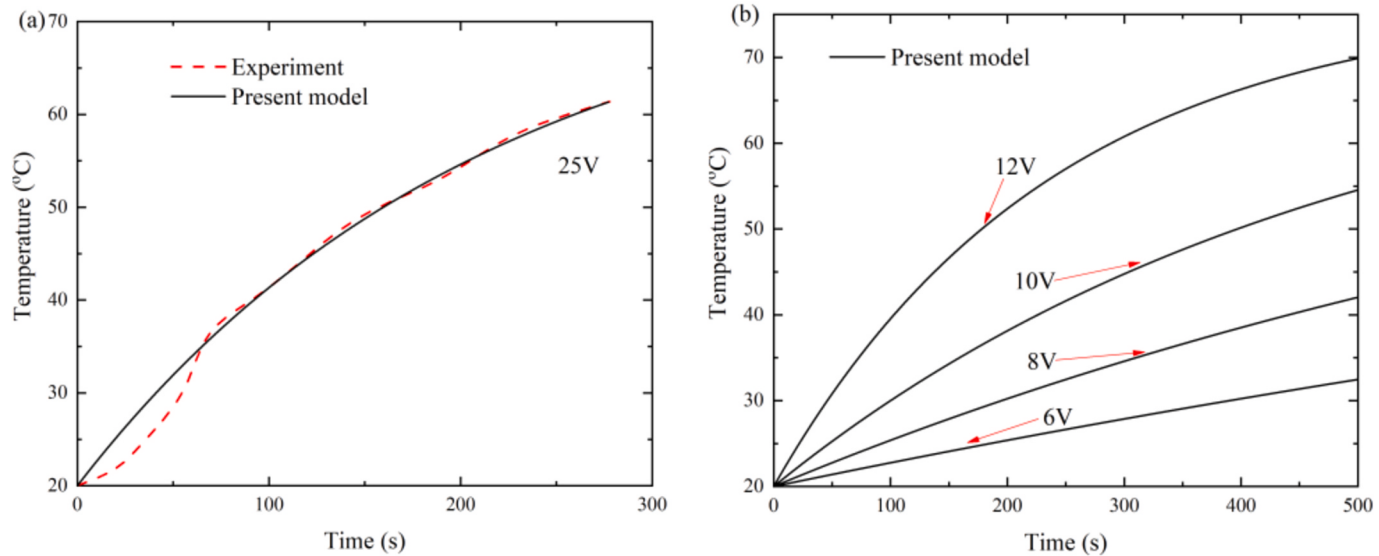


Fig. 17. Effect of applied voltages on surface temperature of SMP [43].

Table 5

Model parameters fitted by the thermo-mechanical experiments of 4D-printed SMP sample [1].

Parameters	Values	Parameters	Values
T_g	63 °C	ρ	1050 kg/m ³
μ_r	2.2 MPa	n_g	50 MPa/s
λ_L	4.0	ΔG	4.0×10^{-20} J
Q_s	2979 K	C_1	12.9
ν	0.4	C_2	39 °C
k_0	0.65×10^{-4} /°C	τ_0	0.3s
B	30000J/kg	η_{ref}	3.0J/Kg·K
C_{p0}	50J/Kg·K	κ	1.0
e	1.39×10^{-9} J/Kg·K	d	1.53×10^{-17} J/Kg
w_t	1.0×10^{-16} kg/m ³	v_t	5.0×10^{-16} kg/m ³
T_{ref}	25 °C	E	1300 MPa
s_0, s_s	29.5 MPa, 12 MPa	h_0	115 MPa

60 min. The relevant parameters are shown in Table 2.

3.3.2. Example 3: experiments cited from Castro et al. [40]

The experiments reported by Castro et al. [40] are also used to verify the model in this section. The SMP material ($T_g = 75$ °C) is an epoxy-based polymer (VFE1-62).

The isothermal compression experiments were conducted at temperatures of 313 K, 353 K and 373 K using a strain rate of 0.01/s, which is shown in Fig. 9. In the work of Castro et al. [40], the shape memory experiments consist of shape programming, shape fixity and shape recovery. The SMP sample was loaded to a compression strain of 20 % at 373 K or 353 K under a constant strain rate of 0.01/s, followed by a relaxation period of 10 min. Subsequently, the ambient temperature was dropped to 313 K at a rate of 2.5 °C/min and maintained at 313 K for 60

Table 6

Model parameters fitted by the thermo-mechanical experiments of 4D-printed SMP sample [44].

Parameters	Values	Parameters	Values
T_g	55 °C	ρ	1050 kg/m ³
μ_r	1.1 MPa	n_g	4210 MPa/s
λ_L	0.5	ΔG	1.25×10^{-20} J
Q_s	2020K	C_1	17.44
ν	0.4	C_2	51.6 °C
s_s	19 MPa	h_0	100 MPa
E	1660 MPa	s_0	19 MPa

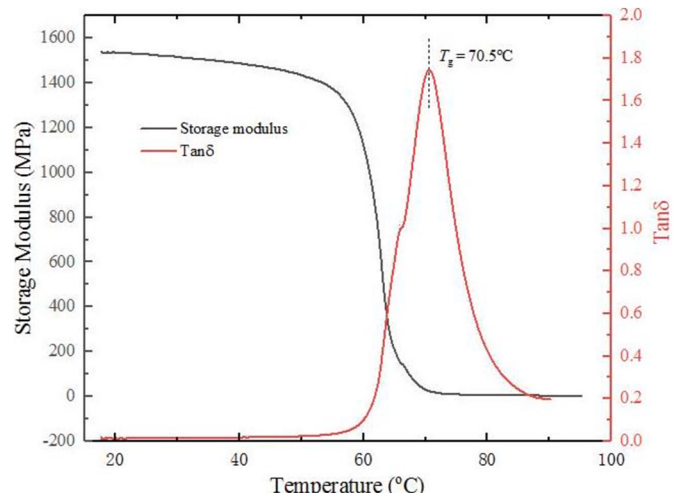


Fig. 18. The testing for the storage modulus and $\tan\delta$ by the DMA machine.

min to achieve shape fixity of the sample. Finally, the ambient temperature was raised to 373 K at a rate of 2.5 °C/min and kept at 373 K for some time to fully restore the original shape of the SMP sample. Note that both experiments were performed using a temperature-controlled MTS Insight 10 universal testing machine. The relevant parameters are shown in Table 2.

3.3.3. Example 4: experiments cited from by Yu et al. [42]

To show the validity of the model for simulating cyclic mechanical response, the experiments reported by Yu et al. [42] are also used to

Table 7

Model parameters fitted by the experiments of 4D-printed SMP sample.

Parameters	Values	Parameters	Values
T_g	70.5 °C	ρ	1050 kg/m ³
μ_r	1.35 MPa	n_g	10123 MPa/s
λ_L	4.0	ΔG	5.0×10^{-20} J
Q_s	7550 K	C_1	17.44
ν	0.4	C_2	51.6 °C
s_s	19.5 MPa	h_0	120 MPa
E	1500 MPa	s_0	53.9 MPa

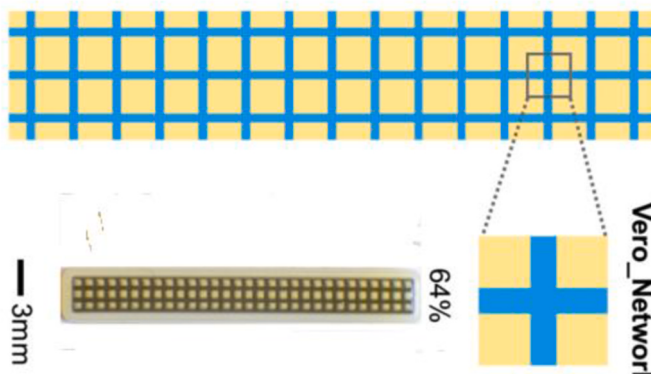


Fig. 19. Design schematics and sample photos of the 4D-printed SMP material [45].

Table 8
Model parameters fitted by the experiments of 4D-printed SMP sample [45].

Parameters	Values	Parameters	Values
T_g	53.5 °C	ρ	1050 kg/m ³
μ_r	0.8 MPa	n_g	50 MPa/s
λ_L	4.0	ΔG	1.5×10^{-19} J
Q_s/s_y	175 K/MPa	C_1	17.44
ν	0.4	C_2	53.65 °C
k_0	$1.1 \times 10^{-4}/^{\circ}\text{C}$	τ_0	3.0s
B	5370J/kg	η_{ref}	6.0J/Kg·K
C_{p0}	60J/Kg·K	κ	1.0
e	$1.5 \times 10^{-9}\text{J/Kg}\cdot\text{K}$	d	$1.5 \times 10^{-17}\text{J/Kg}$
w_t	$1.0 \times 10^{-16}\text{kg/m}^3$	v_t	$5.0 \times 10^{-16}\text{kg/m}^3$
T_{ref}	59 °C	E	790 MPa

verify the model in this section. The SMP material ($T_g = 42.7$ °C) is an acrylate-based network polymer.

In the four-cycle mechanics testing, the material sample was loaded to a tension strain of 10 % using a strain rate of 0.015/min, and subsequently unloaded to 0 strain under the same strain rate. A 15-min interval between each mechanical cycle was set to measure the size in a stable state at room temperature. Note that the cycle testing was conducted at 323 K and 335.7 K, respectively, using the DMA tester. The relevant parameters are shown in Table 3.

3.3.4. Model results comparing to experiments

Fig. 8 shows the effect of the temperatures on the stress-strain responses of epoxy-based SMP under a compressive strain of 20 %. A mechanical phenomenon can be clearly observed, i.e., the transition from the viscoplastic response to the viscoelastic response becomes evident with an increase in temperature.

The model is further applied to examine the impact of both the strain rate and temperature on the stress-strain relationship of acrylate-based SMP under a compressive strain of 40 %, as depicted in Fig. 9. The mechanical phenomenon in Fig. 8 also occur in the acrylate-based SMP. On the other side, the increase in strain rate leads to a substantial enhancement in the yield limit, whereas the softening trends stay nearly constant across various strain rates.

The mechanical responses during a cyclic tension test are also simulated by our model. Fig. 10 shows the tensile stress-strain behavior of SMP in the four cyclic tension tests with a fixed strain of 10 % at two different temperatures of 323 k and 335.7 k. Obviously, the constitutive model reasonably predicts the cyclic stress response.

Fig. 11 compares the shape recovery response represented by the present model with the experimental data and the simulation from the multi-branch model (Westbrook et al. [15]). The two constitutive models can provide successful predictions. However, the results from

the multi-branch model may slightly outperform those from the present model. It is noted that our single-branch model is more concise, making it easier to understand and calculate. Thus, the present model still has certain advantages.

Fig. 12 presents the strain recovery response of SMP materials with different temperature stimuli. In general, the model result closely matches the experimental data. However, the shape recovery simulated by the present model starts slower in the early stage. This phenomenon can be attributed to the hysteresis of the viscous flow rule in the glassy state. The effects of synergistic-relaxation on thermo-mechanical responses are also studied in Fig. 13 in this section. It is clear that the effects are similar to those in Fig. 7.

3.4. Verification III

3.4.1. Example 5: experiments cited from Ozdemir et al. [43]

This section references the electro-thermo-mechanical experiments of SMP material conducted by Ozdemir et al. [43] to examine the model's application in multiphysics problems. The material composition comprises SMP matrix and carbon nanopaper (CNP), as illustrated in Fig. 14. The matrix material ($T_g = 55$ °C) is a polyurethane-based polymer (MP-5510). The CNP layer demonstrates high conductivity, enabling the CNP-SMPC to achieve SME upon the application of voltage.

The electrothermal shape memory cycle comprises shape programming, shape fixity, and shape recovery. The material sample was elongated by 1 % over 100 s at 328 K (achieved with an applied voltage of 20–22 V), followed by a 100-s hold with power disengaged. Thereafter, the material was naturally cooled to 293 K over a duration of 1800 s. The unloading rate was 4 N/s until the load diminished to zero, after which it persisted in a zero stress state for 1000 s at 293 K. The actuation voltage of 25 V was supplied for approximately 300 s to facilitate form recovery. The required model parameters are listed in Table 4.

3.4.2. Electrothermal model

In this section, an electrothermal coupling model is built. The heat required for the temperature change of the sample originates from the electrified CNP layer. According to the Joule's first law, an equation be concluded,

$$\frac{dQ}{dt} = \frac{U^2(t)}{R_{\text{CNP}}} = \frac{U^2}{(L_{\text{CNP}}^2 / (r_{\text{CNP}} V_{\text{CNP}}))} \quad (33)$$

where R_{CNP} , U , L_{CNP} , r_{CNP} and V_{CNP} represent the resistance, applied voltage, length, volume and electrical conductivity of the CNP, respectively. Note that the temperatures of polymer matrix and CNP are assumed to be consistent. Electric energy is transformed into thermal energy of the functional phase (CNP) and the SMP matrix,

$$\gamma_0 \frac{U^2}{(L_{\text{CNP}}^2 / (r_{\text{CNP}} V_{\text{CNP}}))} = \rho_{\text{CNP}} C_{\text{pCNP}} V_{\text{CNP}} \frac{dT}{dt} + \gamma \frac{A_c}{H_m} (T - T_0) k_m \quad (34)$$

where ρ_{CNP} and C_{pCNP} are the density and specific heat capacity of the CNP, respectively. γ_0 represents the probability of electric energy converting into thermal energy. A_c is the contact area. H_m and k represent the thickness and thermal conductivity of the matrix, respectively. The following equation can be obtained using the constant variation method to solve Eq. (34),

$$\frac{dT}{dt} = -K_1 \gamma \frac{A_c k_m}{\rho_{\text{CNP}} C_{\text{pCNP}} V_{\text{CNP}} H_m} \exp\left(-\gamma \frac{A_c k_m}{\rho_{\text{CNP}} C_{\text{pCNP}} V_{\text{CNP}} H_m} t\right) \quad (35)$$

where $\gamma = 1 / ((U^2 r_{\text{CNP}} V_{\text{CNP}} / L_{\text{CNP}}^2) / (\rho_{\text{CNP}} C_{\text{pCNP}} V_{\text{CNP}}))$ is a physical correction factor, K_1 takes a value of -56.5.

3.4.3. Model results comparing to experiments

Fig. 15 illustrates the stress and strain responses of electrothermal shape memory polymer materials across a complete form memory cycle.

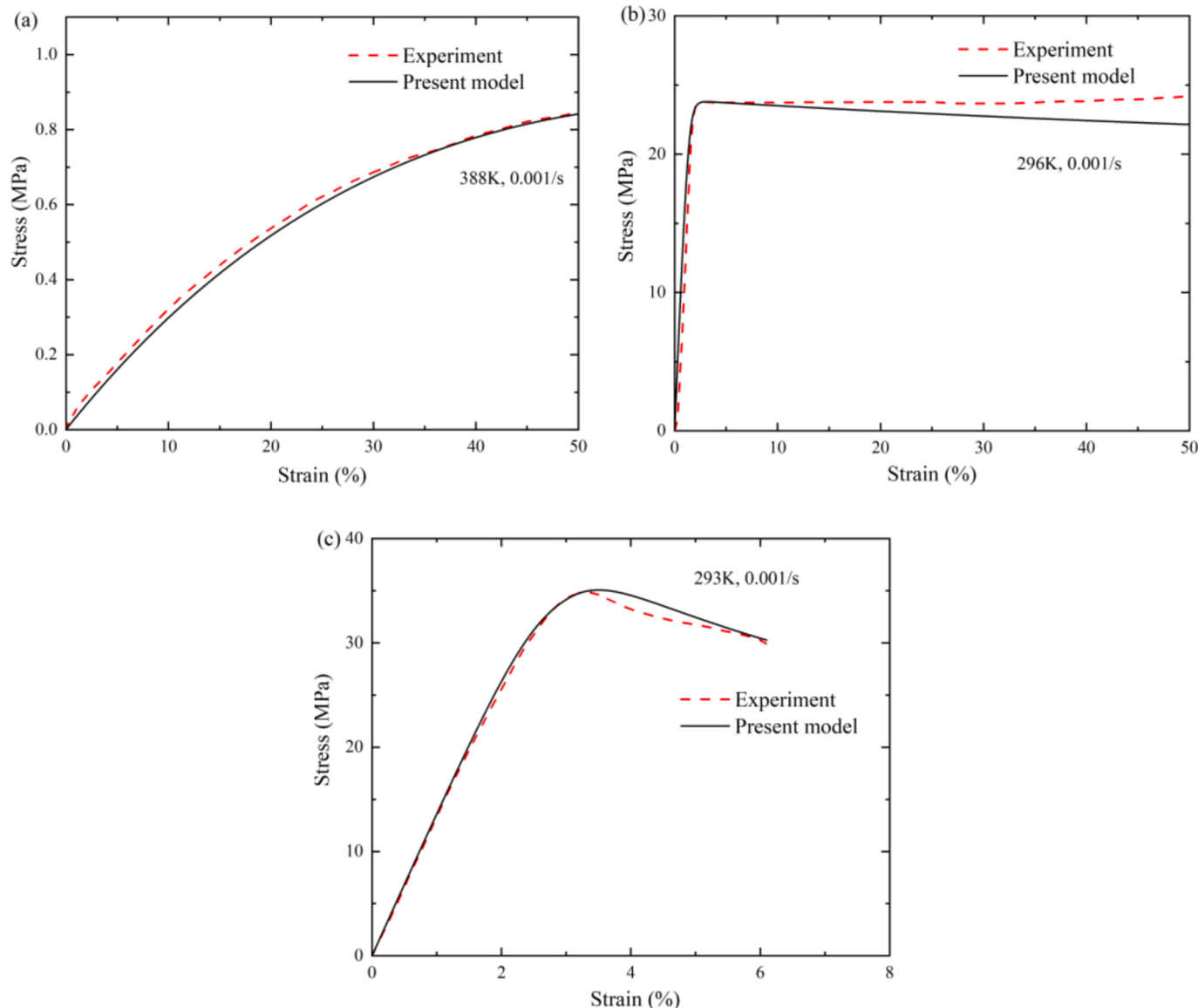


Fig. 20. The stress–strain response of 4D-printed SMP under (a) finite deformation [44] above T_g , (b) finite deformation [44] below T_g and (c) small deformation [1] below T_g .

The model underestimates the stress during the cooling stage seen in Fig. 15a. As shown in Fig. 15b, the mismatch arises from the differing cooling methods employed in theoretical calculations (uniform speed) and practical testing (natural convection). Nonetheless, the stress development features induced by cooling hardening are effectively represented by our constitutive model.

In the electrothermally-driven shape recovery process, material deformation initially increases before progressively diminishing, rather than immediately reverting to its original state, as illustrated in Fig. 16a. The primary reason may be that the strain recovery was excessively overcompensated by thermal expansion in the early stage. The recovery feature is effectively captured by the constitutive model, and the model outcomes demonstrate strong alignment with experimental data. Fig. 16b presents the impact of synergistic relaxation on the strain response. Complete shape recovery is challenging without accounting for synergistic relaxing. Overall, the constitutive model efficiently reproduces the stress and strain responses in the electro-thermo-mechanical cycle.

It is essential to investigate the influence of applied voltages on the surface temperature of SMPs for electrothermally-triggered SMEs. The

temperature during electrothermal actuation is plotted in Fig. 17. Fig. 17b clearly shows a rise in temperature with an applied voltage.

3.5. Verification IV

To study the thermo-mechanical behaviors in 4D-printed SMP materials, multiple sets of experimental data are cited in this section.

3.5.1. Example 6: experiments cited from Zeng et al. [1]

The polylactide acid (PLA)-based SMP ($T_g = 63^\circ\text{C}$) sample was selected for the uniaxial tensile experiment at a temperature and strain rate of 293 K and 0.001/s, respectively. The required model parameters are listed in Table 5.

3.5.2. Example 7: experiments cited from Bodaghi et al. [44]

The polyurethane-based SMP material ($T_g = 55^\circ\text{C}$) was selected for the experimental sample. The uniaxial tensile testing environment is a rubbery temperature of 388 K and a glassy temperature of 296 K, respectively, using a strain rate of 0.001/s. Table 6 shows the required parameters.

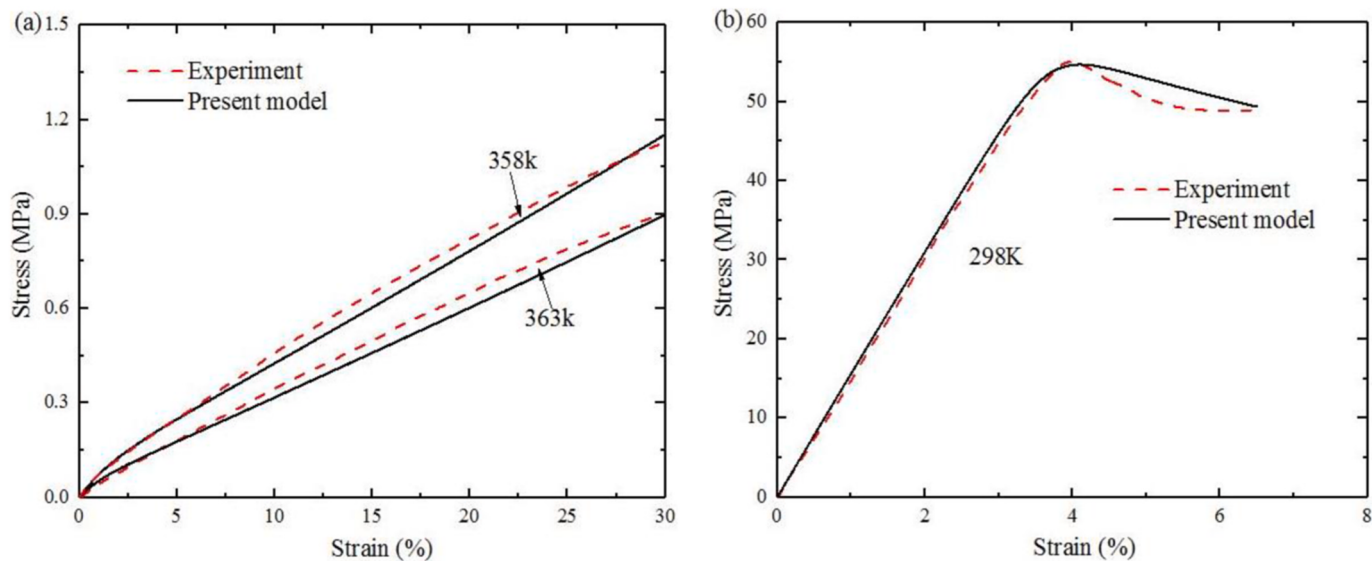


Fig. 21. The stress–strain responses of 4D-printed SMP at (a) rubbery temperature and (b) glassy temperature using a strain rate 0.001/s.

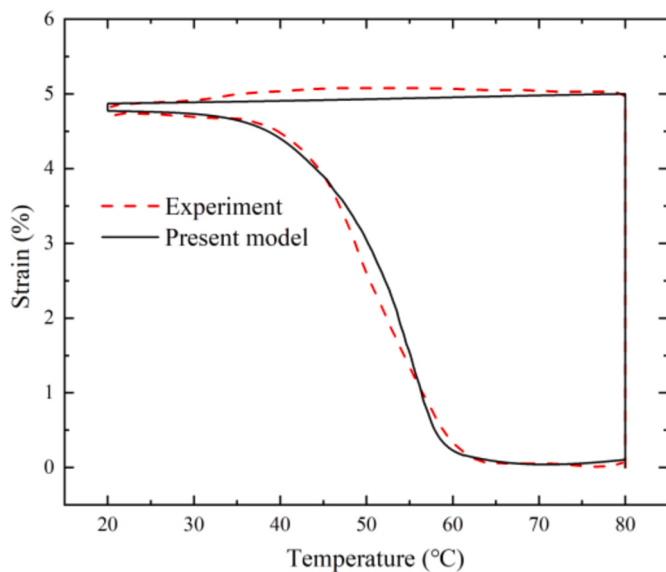


Fig. 22. Temperature-dependent strain response of 4D-printed SMP material [45] in a full shape memory cycle.

3.5.3. Example 8: experiments done by this article authors

In this section, the selected material is PLA-based SMP ($T_g = 70.5^\circ\text{C}$). T_g is determined as the temperature corresponding to the peak value of $\tan\delta$ in a Dynamic Mechanical Analysis (DMA) test shown in Fig. 18. A constant strain rate of 0.06/min is used for the uniaxial tensile tests of the 4D-printed SMP sample at both rubbery and glassy temperatures. Both the experimental data and the model results are plotted in Fig. 21. The required parameters are listed in Table 7.

3.5.4. Example 9: experiments cited from Yuan et al. [45]

Two commercial materials, VeroBlack (64 %) and TangoPlus (36 %), make up the SMP materials ($T_g = 53.5^\circ\text{C}$), as shown in Fig. 19. To achieve a complete shape memory cycle, the material sample was first programmed to a uniaxial tensile strain of 5 % at 353 K within 10 min. Subsequently, the sample temperature was decreased to 293 K at 2 °C/min. Then, the external force was instantaneously unloaded to obtain a temporary shape. Finally, the sample temperature was uniformly

increased to 353 K in 30min to trigger shape recovery. The relevant parameters are shown in Table 8.

3.5.5. Model results comparing to experiments

The 4D-printed SMP's stress-strain responses are shown in Fig. 20 under different temperatures and shapes using a tensile strain rate of 0.001/s. The constitutive model can effectively simulate stress responses at different temperatures and deformation scales. But there isn't any noticeable strain-softening in the low-temperature tension under finite deformation, and the model can't accurately predict how the 4D-printed SMP will behave in terms of direct strain-hardening below T_g . The reason may be that the regular stretching and extrusion of the chains during printing result in a nearly equal distribution of free volume in different segments [46].

To more systematically study the mechanical responses at different temperatures and strains, uniaxial tensile experiments have been conducted as shown in Fig. 21, also the theoretical predictions. The constitutive can well capture the mechanical responses.

To further investigate the properties of 4D-printed SMP material, the constitutive model is applied to predict the strain response in the shape memory cycle. As shown in Fig. 22, our model can effectively capture the strain response with the significant temperature dependence in the 4D-printed SMP during the cycle process.

Fig. 23 examines the effects of synergistic-relaxation on the mechanical and shape memory responses of 4D-printed SMPs. It is clear that synergistic-relaxation plays an important role in the responses. However, differing from the traditional SMPs, the mechanical response is still affected by the synergistic relaxation effect in the theoretical representation.

4. Conclusions

This paper investigates the relationship between structure and stress relaxation in SMPs. As a result, a thermodynamic constitutive model is proposed that incorporates the synergistic-relaxation effects. A novel electrothermal coupling model is introduced into the constitutive theory framework to further characterize multiphysics field problems. Then, the constitutive model is used to describe the thermo-mechanical behaviors of 4D-printed SMPs and traditional SMPs as well as the electro-thermo-mechanical behaviors. Multiple sets of experiments are applied to validate the constitutive model. Our model can effectively represent the thermo-mechanical and electro-thermo-mechanical responses. Moreover, the synergistic-relaxation effects play an important role in the

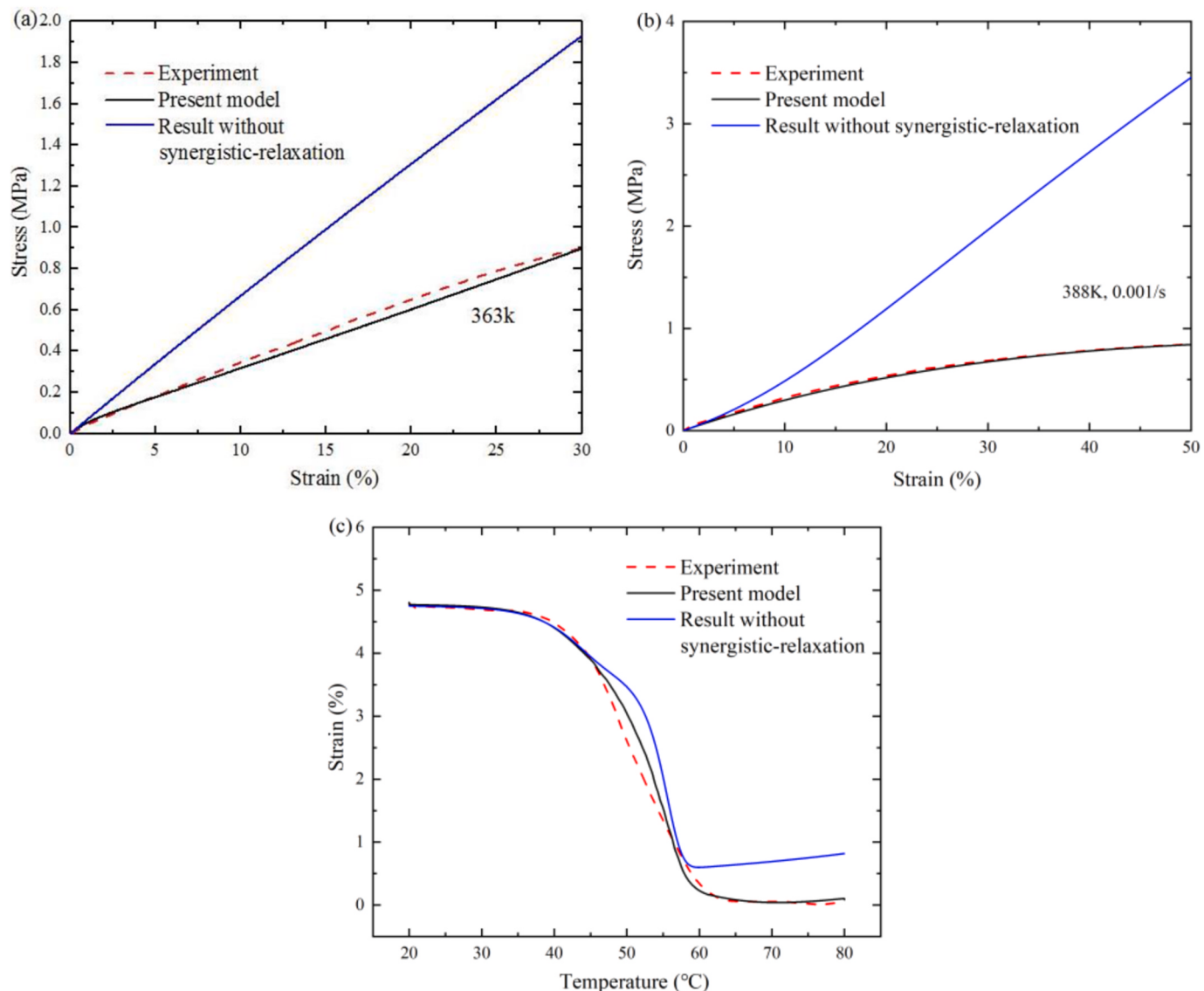


Fig. 23. The effects of synergistic-relaxation on the (a) mechanical response at 363 K, the (b) mechanical response [44] at 388 K and the (c) shape memory response [45] of 4D-printed SMP.

shape recovery process, which can determine the ultimate recovery ratio.

However, the model cannot accurately predict the finite deformation stretching behavior of 4D-printed SMP below T_g , because direct yield-hardening has replaced the conventional yield-softening-hardening process. Thus, in the future, a new yield rule should be developed to describe the unique strain-hardening behavior of 4D-printed SMP. In addition, only the experimental testing of 4D-printed SMPs is shown. Future work should also conduct comprehensive thermo-mechanical experiments and theoretical calculations of 4D-printed shape memory polymer composites (SMPCs).

CRediT authorship contribution statement

Hao Duan: Writing – original draft, Validation, Software, Methodology, Investigation, Formal analysis, Data curation. **Huiyu Sun:**

Writing – review & editing, Visualization, Supervision, Resources, Project administration, Funding acquisition, Conceptualization. **Jesus A. Rodriguez-Morales:** Software, Methodology. **Xinyuan Bai:** Software, Methodology.

Declaration of competing interest

The authors declare that they have no known competing financial interests or personal relationships that could have appeared to influence the work reported in this paper.

Acknowledgments

This work is supported by the National Natural Science Foundation of China (Grant Nos.: 12372071) and the Aeronautical Science Fund (Grant No.:2022Z055052001).

Appendix A. Thermodynamic consideration

The entire Helmholtz free energy of SMPs can be broken down into five components using the constitutive model's rheological description as a

basis:

$$\Psi = W_M(\mathbf{C}_M, T) + W_e(\mathbf{C}_e, T) + W_T(T) \quad (\text{A.1})$$

where W_M and W_e stand for the contributions of free energy caused by the hyperelastic and viscoelastic components, respectively. W_T is the contribution of free energy caused by temperature. The time derivative at both ends of Eq. (A.1) is written as,

$$\frac{d\Psi}{dt} = \frac{\partial W_M}{\partial \mathbf{C}_M} : \frac{d\mathbf{C}_M}{dt} + \frac{\partial W_e}{\partial \mathbf{C}_e} : \frac{d\mathbf{C}_e}{dt} + \frac{\partial W_T}{\partial T} \frac{dT}{dt} \quad (\text{A.2})$$

The way to express the second law of thermodynamics can be written as an inequality,

$$\frac{d\Psi}{dt} + \mathcal{S} : \frac{d\mathbf{E}_M}{dt} - \frac{dT}{dt} \eta - \frac{\nabla T \cdot \mathbf{q}}{T} \geq 0 \quad (\text{A.3})$$

where \mathcal{S} , η , and \mathbf{q} are the second Piola-Kirchhoff stress tensor, the entropy, and the heat flux vector, respectively. ∇ is the gradient operator. With consideration of Eqs. (7) and (8), Eq. (A.2) is substituted into Eq. (A.3), leading to the following inequality.

$$\begin{aligned} \frac{1}{2} \left(\mathcal{S} - 2 \frac{\partial W_M}{\partial \mathbf{C}_M} - 2 \mathbf{F}_v^{-1} \cdot \frac{\partial W_e}{\partial \mathbf{C}_e} \cdot \mathbf{F}_v^{-T} \right) : \frac{d\mathbf{C}_M}{dt} - \left(\frac{\partial W_e}{\partial \mathbf{C}_e} : \frac{d\mathbf{F}_v}{dt} + \frac{\partial W_e}{\partial \mathbf{C}_e} : \frac{d\mathbf{F}_v^T}{dt} \right) \\ - \left(\frac{\partial W_M}{\partial T} + \frac{\partial W_e}{\partial T} + \frac{\partial W_T}{\partial T} + \eta \right) \frac{dT}{dt} - \mathbf{q} \cdot \nabla T / T \geq 0 \end{aligned} \quad (\text{A.4})$$

To satisfy arbitrary thermodynamic processes, the following equations can be obtained,

$$\mathcal{S} = 2 \frac{\partial W_M}{\partial \mathbf{C}_M} + 2 \mathbf{F}_v^{-1} \frac{\partial W_e}{\partial \mathbf{C}_e} \cdot \mathbf{F}_v^{-T} \quad (\text{A.5})$$

The Cauchy stress equals,

$$\boldsymbol{\sigma} = \frac{1}{J_M} \mathbf{F}_M \cdot \mathcal{S} \cdot \mathbf{F}_M^T \quad (\text{A.6})$$

$$\boldsymbol{\sigma} = \frac{2}{J_M} \left(\frac{\partial W_M}{\partial \mathbf{C}_M} + \mathbf{F}_v^{-1} \cdot \frac{\partial W_e}{\partial \mathbf{C}_e} \cdot \mathbf{F}_v^{-T} \right) \quad (\text{A.7})$$

where $J_M = \det [\mathbf{F}_M]$.

The hyperelastic behaviors can be well captured by the energy function reported in the literature [31],

$$W_M(\mathbf{C}_M, T) = \mu_r \left(\lambda_L \lambda_{\text{eff}} L^{-1} \left(\frac{\lambda_{\text{eff}}}{\lambda_L} \right) + \lambda_L^2 \ln \left(L^{-1} \left(\frac{\lambda_{\text{eff}}}{\lambda_L} \right) / \sinh L^{-1} \left(\frac{\lambda_{\text{eff}}}{\lambda_L} \right) \right) \right) \quad (\text{A.8})$$

where μ_r , λ_L and λ_{eff} are the initial shear modulus, the locking stretch, and the effective chain stretch, respectively. The stress response of the implicit spring is characterized by a neo-Hookean form of strain energy function,

$$W_e(\mathbf{C}_e, T) = \frac{G_e}{2} (\bar{I}_e - 3) \quad (\text{A.9})$$

where G_e is the effective stiffness of the implicit spring in the viscoelastic part. Substituting Eq. (A.9) and (A.8) into (A.7) yields Eqs. (9)–(11) in section 2.2. Eq. (11) can be further reduced as follows:

$$\boldsymbol{\sigma} = \frac{\lambda_1^2 - \lambda_2 \lambda_3}{(J_M)^{5/3}} \mu_r \frac{\lambda_L}{\lambda_{\text{eff}}} L^{-1} \left(\frac{\lambda_{\text{eff}}}{\lambda_L} \right) \begin{bmatrix} 2 & 0 & 0 \\ 0 & -1 & 0 \\ 0 & 0 & -1 \end{bmatrix} + \frac{(\lambda_{e1})^2 - \lambda_{e2} \lambda_{e3}}{J_M (J_e)^{2/3}} G_e \begin{bmatrix} 2 & 0 & 0 \\ 0 & -1 & 0 \\ 0 & 0 & -1 \end{bmatrix} \quad (\text{A.10})$$

where λ_1 is the axial deformation direction (\mathbf{n}_1). λ_2 is equal to λ_3 , which represent the other directions in a rectangular coordinate system (\mathbf{n}_2 and \mathbf{n}_3). λ_{e1} and λ_{e2} ($\lambda_{e2} = \lambda_{e3}$) represent the elastic stretches of the implicit spring.

Data availability

Data will be made available on request.

References

- [1] C.J. Zeng, L.W. Liu, Y.Q. Hu, W.F. Bian, J.S. Leng, Y.J. Liu, A viscoelastic constitutive model for shape memory polymer composites: micromechanical modeling, numerical implementation and application in 4D printing, *Mech. Mater.* 169 (2022) 104301, <https://doi.org/10.1016/j.mechmat.2022.104301>.
- [2] C.J. Zeng, L.W. Liu, Y.Q. Hu, W.F. Bian, J.S. Leng, Y.J. Liu, Temperature-dependent mechanical response of 4D printed composite lattice structures reinforced by continuous fiber, *Compos. Struct.* 280 (2022) 114952, <https://doi.org/10.1016/j.compositstruct.2021.114952>.
- [3] W. Small, P. Singhal, T.S. Wilson, D.J. Maitland, Biomedical applications of thermally activated shape memory polymers, *J. Mater. Chem. B* 20 (2010) 3356–3366, <https://doi.org/10.1039/B923717H>.
- [4] M. Baghani, R. Dolatabadi, M. Baniassadi, Developing a finite element beam theory for nanocomposite shape memory polymers with application to sustained release of drugs, *Sci. Iran.* 24 (2017) 249–259, <https://doi.org/10.24200/SCI.2017.4030>.
- [5] A. Lendlein, H.Y. Jiang, O. Jangler, R. Langer, Light induced shape-memory polymers, *Nature* 434 (2005) 879–882, <https://doi.org/10.1002/adma.200502266>.
- [6] K.N. Long, T.F. Scott, H.J. Qi, C.N. Bowman, M.L. Dunn, Photomechanics of light-activated polymers, *J. Mech. Phys. Solid.* 57 (2009) 1103–1121, <https://doi.org/10.1016/j.jmps.2009.03.003>.

- [7] Y.J. Liu, H.B. Lv, X. Lan, J.S. Leng, S.Y. Du, Review of electro-active shape-memory polymer composite, *Compos. Sci. Technol.* 69 (2009) 2064–2068, <https://doi.org/10.1016/j.compscitech.2008.08.016>.
- [8] H.B. Lv, Y.T. Yao, L. Lin, Carbon-based reinforcement in shape-memory polymer composite for electrical actuation, *Pigment Resin Technol.* 43 (2014) 26–34, <https://doi.org/10.1108/PRT-08-2013-0075>.
- [9] P.R. Buckley, G.H. McKinley, T.S. Wilson, W. Small, W.J. Bennett, J. Bearinger, M.W. McElfresh, D.J. Maitland, Inductively-heated shape memory polymer for the magnetic actuation of medical devices, *IEEE Trans. Biomed. Eng.* 53 (2006) 2075–2083, <https://doi.org/10.1109/TBME.2006.877113>.
- [10] S. Conti, M. Lenz, M. Rumpf, Modeling and simulation of magnetic-shape-memory polymer composites, *J. Mech. Phys. Solid.* 55 (2007) 1462–1486, <https://doi.org/10.1016/j.jmps.2006.12.008>.
- [11] T.D. Nguyen, H.J. Qi, F. Castro, K.N. Long, A thermoviscoelastic model for amorphous shape memory polymers: incorporating structural and stress relaxation, *J. Mech. Phys. Solid.* 56 (9) (2008) 2792–2814, <https://doi.org/10.1016/j.jmps.2008.04.007>.
- [12] T.D. Nguyen, C.M. Yakacki, P.D. Brahmbhatt, M.L. Chambers, Modeling the relaxation mechanisms of amorphous shape memory polymers, *Adv. Mater.* 22 (31) (2010) 3411–3423, <https://doi.org/10.1002/adma.200904119>.
- [13] H. Zeng, J.S. Leng, J.P. Gu, H.Y. Sun, A thermoviscoelastic model incorporated with uncoupled structural and stress relaxation mechanisms for amorphous shape memory polymers, *Mech. Mater.* 124 (2018) 18–25, <https://doi.org/10.1016/j.mechmat.2018.05.010>.
- [14] J.P. Gu, H.Y. Sun, C.Q. Fang, A finite deformation constitutive model for thermally activated amorphous shape memory polymers, *J. Intell. Mater. Syst. Struct.* 26 (2015) 1530–1538, <https://doi.org/10.1177/1045389X14544147>.
- [15] K.K. Westbrook, P.H. Kao, F. Castro, Y.F. Ding, H.J. Qi, A 3D finite deformation constitutive model for amorphous shape memory polymers: a multi-branch modeling approach for nonequilibrium relaxation processes, *Mech. Mater.* 43 (2011) 853–869, <https://doi.org/10.1016/j.mechmat.2011.09.004>.
- [16] R. Xiao, J.W. Choi, N. Lakhera, C.M. Yakacki, C.P. Frick, Thao D. Nguyen, Modeling the glass transition of amorphous networks for shape-memory behavior, *J. Mech. Phys. Solid.* 61 (2013) 1612–1635, <https://doi.org/10.1016/j.jmps.2013.02.005>.
- [17] J.P. Gu, J.S. Leng, H.Y. Sun, A constitutive model for amorphous shape memory polymers based on thermodynamics with internal state variables, *Mech. Mater.* 111 (2017) 1–14, <https://doi.org/10.1016/j.mechmat.2017.04.008>.
- [18] X.B. Su, X.Q. Peng, A 3D finite strain viscoelastic constitutive model for thermally induced shape memory polymers based on energy decomposition, *Int. J. Plast.* 110 (2018) 166–182, <https://doi.org/10.1016/j.ijplas.2018.07.002>.
- [19] Y. Wang, J. Wang, X.Q. Peng, Refinement of a 3D finite strain viscoelastic constitutive model for thermally induced shape memory polymers, *Polym. Test.* 96 (2021) 107139, <https://doi.org/10.1016/j.polymertesting.2021.107139>.
- [20] H. Duan, J.P. Gu, H. Zeng, A.A. Khatibi, H.Y. Sun, A thermoviscoelastic finite deformation constitutive model based on dual relaxation mechanisms for amorphous shape memory polymers, *Int. J. Smart. Nano. Mat.* 14 (2023) 243–264, <https://doi.org/10.1080/19475411.2023.2206675>.
- [21] J.H. Gibbs, G. Adam, On the temperature dependence of cooperative relaxation properties in glass-forming liquids, *J. Chem. Phys.* 43 (1965) 139–146, <https://doi.org/10.1063/1.1696442>.
- [22] P. Ping, W.S. Wang, X.S. Chen, X.B. Jing, Poly(e-caprolactone) polyurethane and its shape-memory property, *Biomacromolecules* 6 (2005) 587–592, <https://doi.org/10.1021/bm049477j>.
- [23] W. Wang, Y. Jin, P. Ping, X. Chen, X. Jing, Z. Su, Structure evolution in segmented poly(ester urethane) in shape-memory process, *Macromolecules* 43 (2010) 2942–2947, <https://doi.org/10.1021/ma902781e>.
- [24] G.Q. Li, W. Xu, Thermomechanical behavior of thermoset shape memory polymer programmed by cold compression: testing and constitutive modeling, *J. Mech. Phys. Solid.* 59 (2011) 1231–1250, <https://doi.org/10.1016/j.jmps.2011.03.001>.
- [25] K. Shahi, R. Boomurugan, R. Velmurugan, Cold programming of epoxy-based shape memory polymer, *Structures* 29 (2021) 2082–2093, <https://doi.org/10.1016/j.struc.2020.05.023>.
- [26] R. Abishera, R. Velmurugan, K.V.N. Gopal, Reversible plasticity shape memory effect in carbon nanotubes reinforced epoxy nanocomposites, *Compos. Sci. Technol.* 137 (2016) 148–158, <https://doi.org/10.1016/j.compscitech.2016.10.030>.
- [27] R. Abishera, R. Velmurugan, K.V.N. Gopal, Reversible plasticity shape memory effect in epoxy/CNT nanocomposites—a theoretical study, *Compos. Sci. Technol.* 141 (2017) 145–153, <https://doi.org/10.1016/j.compscitech.2017.01.020>.
- [28] H. Zeng, J.S. Leng, J.P. Gu, H.Y. Sun, Modeling the thermo-mechanical behaviors of shape memory polymers and their nanocomposites by a network transition theory, *Smart. Mater. Struct.* 28 (2019) 065018, <https://doi.org/10.1088/1361-665X/ab1156>.
- [29] L. Dai, C. Tian, R. Xiao, Modeling the thermo-mechanical behavior and constrained recovery performance of cold-programmed amorphous shape-memory polymers, *Int. J. Plast.* 127 (2020) 102654, <https://doi.org/10.1016/j.ijplas.2019.102654>.
- [30] H. Duan, J.P. Gu, H.Y. Sun, H. Zeng, A multi-scale thermodynamic model incorporated with a single stress relaxation mechanism for polymer-based shape memory nanocomposites, *Mater. Today Commun.* 39 (2024) 109307, <https://doi.org/10.1016/j.mtcomm.2024.109307>.
- [31] E.M. Arruda, M.C. Boyce, A three-dimensional constitutive model for the large stretch behavior of rubber elastic materials, *J. Mech. Phys. Solid.* 41 (1993) 389–412, [https://doi.org/10.1016/0022-5096\(93\)90013-6](https://doi.org/10.1016/0022-5096(93)90013-6).
- [32] G.A. Holzapfel, *Nonlinear Solid Mechanics: a Continuum Approach for Engineering*, 2002.
- [33] A. Lion, J. Peters, S. Kolmeyer, Simulation of temperature history-dependent phenomena of glass-forming materials based on thermodynamics with internal state variables, *Thermochim. Acta* 522 (2011) 182–193, <https://doi.org/10.1016/j.tca.2010.12.017>.
- [34] A. Lion, B. Yagimli, On the frequency-dependent specific heat and TMDSC: constitutive modelling based on thermodynamics with internal state variables, *Thermochim. Acta* 490 (2009) 64–74, <https://doi.org/10.1016/j.tca.2009.02.016>.
- [35] E.M. Arruda, M.C. Boyce, Evolution of plastic anisotropy in amorphous polymers during finite straining, *Int. J. Plast.* 9 (1993) 697–720, [https://doi.org/10.1016/0749-6419\(93\)90034-N](https://doi.org/10.1016/0749-6419(93)90034-N).
- [36] X. Wang, Y. Liu, H. Lu, Y.Q. Fu, On the free-volume model of multi-shape memory effect in amorphous polymer, *Smart. Mater. Struct.* 28 (2019) 125012, <https://doi.org/10.1088/1361-665X/ab500e>.
- [37] P.B. Macedo, T.A. Litovitz, On the relative roles of free volume and activation energy in the viscosity of liquids, *J. Chem. Phys.* 42 (1965) 245–256, <https://doi.org/10.1063/1.1695683>.
- [38] A.K. Doolittle, Studies in Newtonian flow: II. The dependence of the viscosity of liquids on free-space, *J. Appl. Phys.* 22 (1951) 1471, <https://doi.org/10.1063/1.1699894>.
- [39] M.C. Boyce, G.G. Weber, D.M. Parks, On the kinematics of finite strain plasticity, *J. Mech. Phys. Solid.* 37 (1989) 647–665, [https://doi.org/10.1016/0022-5096\(89\)90033-1](https://doi.org/10.1016/0022-5096(89)90033-1).
- [40] F. Castro, K.K. Westbrook, J. Hermiller, D.H. Ahn, Y.F. Ding, H.J. Qi, Time and temperature dependent recovery of epoxy-based shape memory polymers, *J. Eng. Mater-T. Asme.* 133 (2011), <https://doi.org/10.1115/1.4003103>.
- [41] F. Wang, C. Yuan, D. Wang, D.W. Rosen, Q. Ge, A phase evolution based constitutive model for shape memory polymer and its application in 4D printing, *Smart. Mater. Struct.* 29 (2020) 055016, <https://doi.org/10.1088/1361-665X/ab7ab0>.
- [42] K. Yu, Q. Ge, H.J. Qi, Effects of stretch induced softening to the free recovery behavior of shape memory polymer composites, *Polymer* 55 (2014) 5938–5947, <https://doi.org/10.1016/j.polymer.2014.06.050>.
- [43] V.B. Ozdemir, k. Kwok, Electro-thermo-mechanical behavior of carbon nanopaper shape memory polymer composites, *J. Intell. Mater. Syst. Struct.* 33 (2022) 489–500.
- [44] M. Bodaghi, A.R. Damanpakk, W.H. Liao, Triple shape memory polymers by 4D printing, *Smart. Mater. Struct.* 27 (2018) 065010, <https://doi.org/10.1088/1361-665X/abbc2a>.
- [45] C. Yuan, F. Wang, B. Qi, Z. Ding, D.W. Rosen, Q. Ge, 3D printing of multi-material composites with tunable shape memory behavior, *Mater. Des.* 193 (2020) 108785, <https://doi.org/10.1016/j.matdes.2020.108785>.
- [46] S.V. Jatin, S. Basu, Investigations into the origins of plastic flow and strain hardening in amorphous glassy polymers, *Int. J. Plast.* 56 (2014) 139–155, <https://doi.org/10.1016/j.ijplas.2013.11.007>.